Journal of Asian Earth Sciences 143 (2017) 249–268

Contents lists available at ScienceDirect

Journal of Asian Earth Sciences

journal homepage: www.elsevier.com/locate/jseaes

Early Jurassic calc-alkaline magmatism in northeast China: Magmatic response to subduction of the Paleo-Pacific Plate beneath the Eurasian continent

Feng Wang[a,b,*], Yi-Gang Xu[a], Wen-Liang Xu[b,c], Lei Yang[d], Wei Wu[a], Chen-Yang Sun[b]

[a] State Key Laboratory of Isotope Geochemistry, Guangzhou Institute of Geochemistry, Chinese Academy of Sciences, Guangzhou 510640, PR China
[b] College of Earth Sciences, Jilin University, Changchun 130061, PR China
[c] State Key Laboratory of Geological Processes and Mineral Resources, China University of Geosciences, Wuhan 430074, PR China
[d] State Key Laboratory of Lithospheric Evolution, Institute of Geology and Geophysics, Chinese Academy of Sciences, Beijing 100029, PR China

ARTICLE INFO

Keywords:
Early Jurassic
Calc-alkaline igneous rocks
Zircon U–Pb dating
Geochemistry
Petrogenesis
NE China
Paleo-Pacific Plate subduction

ABSTRACT

The subduction of the Paleo-Pacific Plate played an important role in the regional evolution of the eastern margin of the Eurasian continent, but the timing and extent of this event remain ambiguous. To address these issues, we examine the geochronology and geochemistry of Early Jurassic intrusive rocks in eastern Jilin Province, NE China. The Early Jurassic gabbro–diorites, diorites, granodiorites, and monzogranites are found to have been emplaced at 183–185 Ma and are characterized by enrichment in large ion lithophile elements and depletion in high field strength elements, similar to calc-alkaline arc-type igneous rocks. The Early Jurassic gabbroic and dioritic rocks have $\varepsilon Hf_{(t)}$ values of +2.1 to +10.1 and Hf single-stage (T_{DM1}) model ages of 430–774 Ma, whereas the monzogranites have $\varepsilon Hf_{(t)}$ values of +6.7 to +8.9 and Hf single-stage (T_{DM1}) ages of 597–718 Ma. The gabbro–diorites, diorites, and granodiorites described in this study are genetically linked and they represent the products of the fractional crystallization of a common mafic magma that was in turn derived from the partial melting of a mantle source that was metasomatized by subduction-related fluids. In contrast, the Early Jurassic monzogranites were generated by partial melting of a depleted lower crustal block that was probably accreted during the Neoproterozoic. More importantly, the Early Jurassic calc-alkaline igneous rocks in the east part of NE China form a NE-trending belt that is oriented perpendicular to the direction of Paleo-Pacific Plate movement at that time. West of this belt, contemporaneous bimodal igneous rocks occur in the Lesser Xing'an–Zhangguangcai Ranges. This magmatic configuration is best explained by continental arc magmatism along the continental margin and extensional magmatism in a back-arc setting, in each case triggered by the initial subduction of the Paleo-Pacific Plate beneath Eurasia in the Early Jurassic.

1. Introduction

Subduction of the Paleo-Pacific Plate beneath Eurasia had a strong influence on the Mesozoic tectonic evolution of the eastern margin of the Eurasian continent and contributed to the formation of a mineralized belt in the region (Chen et al., 2012; Xu et al., 2013a, 2013b; Deng et al., 2014). The timing of the onset of this subduction remains debated. While the majority of researchers agree that subduction began during the Early–Middle Jurassic (Zhao et al., 1994; Sun et al., 2005; Wu et al., 2007a; Pei et al., 2008; Zhou et al., 2009; Yu et al., 2012; Xu et al., 2013a; Guo et al., 2015), others have suggested it started in the Triassic (Zhao et al., 1996; Zhou et al., 2014; Wilde, 2015; Yang et al., 2015) or even the early Permian (Ernst et al., 2007; Sun et al., 2015). These disagreements arise from the superimposition of two major regional tectonic events, one related to subduction of the Paleo-Pacific Plate (JBGMR, 1988; HBGMR, 1993; Zhao et al., 1994, 1996; He et al., 1998; Sun et al., 2005; Wu et al., 2007a; Pei et al., 2008; Zhou et al., 2009; Xu et al., 2013a, 2013b; Xu, 2014) and the other related to the earlier closure of the Paleo-Asian Ocean (Sengör et al., 1993; Li, 1998, 2006; Li et al., 2007; Wu et al., 2002, 2007a, 2011; Xiao et al., 2003; Sun et al., 2004; Zhang et al., 2004, 2009; Xu et al., 2009; Zhao et al., 2010; Peng et al., 2012; Cao et al., 2013; Wang et al., 2015). The discrimination of the geological records of these two tectonic regimes is critical in order to establish the timing of the initiation of subduction of the Paleo-Pacific Plate beneath the eastern Asian continent.

Recent studies have suggested that the final closure of the Paleo-

* Corresponding author at: 2199 Jianshe Street, College of Earth Sciences, Jilin University, Changchun 130061, PR China.
E-mail address: jlu_wangfeng@jlu.edu.cn (F. Wang).

http://dx.doi.org/10.1016/j.jseaes.2017.04.018
Received 7 September 2016; Received in revised form 19 April 2017; Accepted 19 April 2017
Available online 25 April 2017
1367-9120/

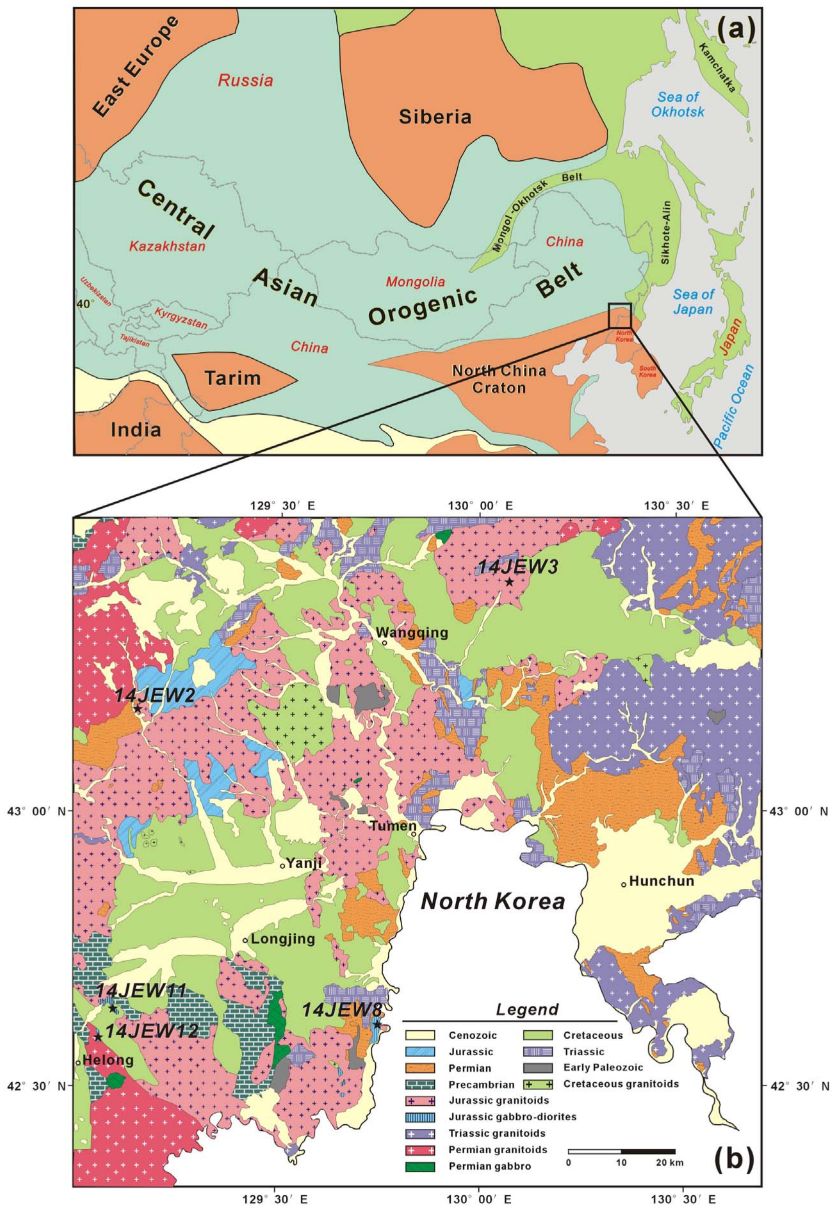

Fig. 1. (a) General map showing the location of the study area, modified after Safonova and Santosh (2014). (b) Detailed geological map of eastern Jilin Province showing sample locations, modified after JBGMR (2007).

Asian Ocean occurred during the earliest Mesozoic (Zhang et al., 2009; Zhao et al., 2010; Wu et al., 2011; Peng et al., 2012; Cao et al., 2013). Furthermore, the Late Triassic bimodal volcanism in the eastern part of NE China, which records post-orogenic extension related to the final closure of the Paleo-Asian Ocean, indicates that subduction of the Paleo-Pacific Plate beneath Eurasia did not persist beyond the Late Triassic (Xu et al., 2013a; Guo et al., 2015; Wang et al., 2015a). Therefore, the identification of the earliest subduction-related calc-alkaline igneous rocks (i.e., after the Late Triassic) is key to constraining the timing of the initiation of subduction of the Paleo-Pacific Plate.

The eastern part of NE China (including eastern Jilin Province) is characterized by immense volumes of igneous rocks whose rough geochronological framework has only recently been established (Wu et al., 2011; Xu et al., 2013a, 2013b). The region examined in the present study is located in the eastern margin of Eurasia (Fig. 1) and is an ideal area for studying the subduction history of the Paleo-Pacific Plate. However, there are still competing views on the Mesozoic tectonics of NE China, especially with regard to the eastern part of this region (Wu et al., 2011). Furthermore, few studies have examined the geochronology and petrogenesis of mafic intrusions in NE China, largely because these rocks occur only sporadically and are volumetrically small relative to granitoids (Yu et al., 2012; Guo et al., 2015; Wang et al., 2015).

To address this shortcoming, we present new LA–ICP–MS zircon ages and whole-rock geochemical data for Early Jurassic calc-alkaline intrusive rocks from east Jilin Province. These data are used to constrain the Early Jurassic tectonic setting of the area and to support our interpretation that the calc-alkaline magmas formed as a result of subduction of the Paleo-Pacific Plate. Thereby, we constrain the timing of the initiation of subduction of the Paleo-Pacific Plate beneath the Eurasian continent.

2. Geological background and sample descriptions

Tectonically, NE China is considered to represent the eastern segment of the Central Asian Orogenic Belt (CAOB), which is located between the North China Craton (NCC) and the Siberian Craton (Sengör et al., 1993; Sengör and Natal'in, 1996; Li, 2006; Windley et al., 2007;

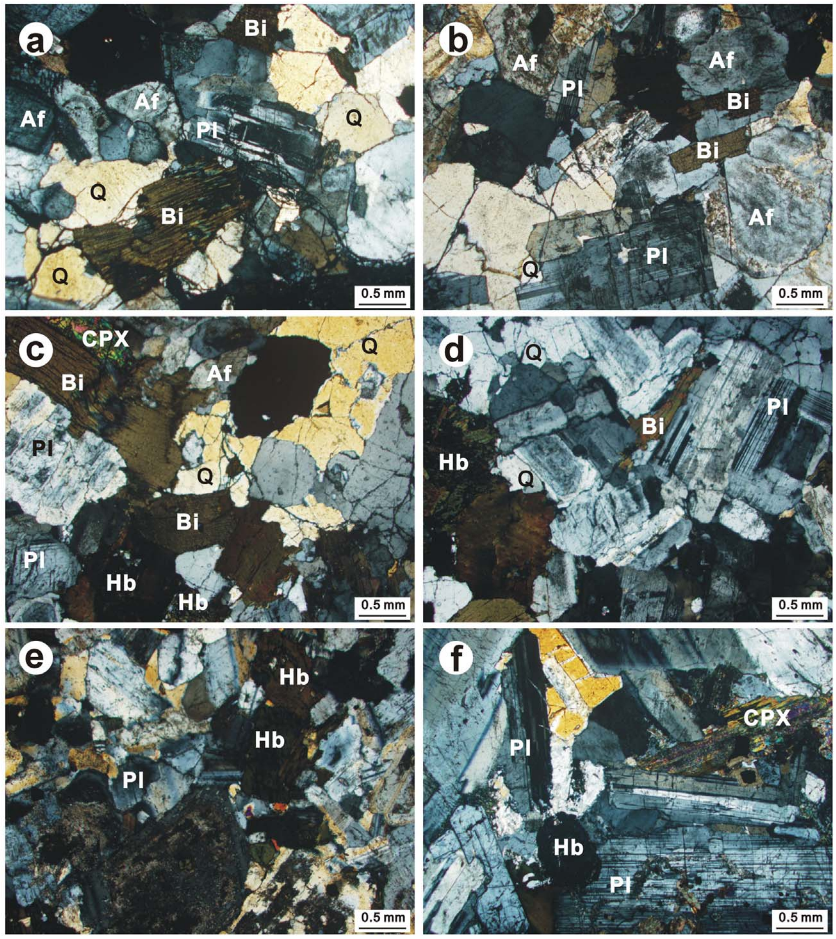

Fig. 2. Photomicrographs of selected samples from the Early Jurassic intrusive rocks (cross-polarized light); (a) sample 14JEW2-1 (granodiorite); (b) sample 14JEW3-1 (monzogranite); (c) sample 14JEW8-1 (diorite); (d) sample 14JEW8-1 (diorite); (e) sample 14JEW11-1 (gabbro-diorite); (f) sample 14JEW12-3 (gabbro-diorite). Af: alkali feldspar, Bi: biotite, Cpx: clinopyroxene, Hb: hornblende, Pl: plagioclase, Q: quartz.

Fig. 1a). NE China is thought to a collage of several microcontinents, including, from southeast to northwest, the Khanka, Jiamusi, Songnen–Zhangguangcai Range, Xing'an, and Erguna massifs (Sengör et al., 1993; Li et al., 1999; Jahn, 2004; Li, 2006). The Paleozoic tectonic evolution of NE China is characterized by the amalgamation of these microcontinental massifs and the final closure of the Paleo-Asian Ocean (Li, 2006; Xu et al., 2009; Wu et al., 2011; Cao et al., 2013), whereas Mesozoic tectonism was related to the circum-Pacific tectonic system (Wu et al., 2011; Xu et al., 2013a, 2013b). The eastern part of Jilin Province is situated at the junction between the eastern segment of the CAOB to the north and the NCC to the south (Fig. 1a), and it consists of metamorphosed Precambrian basement (e.g., the Jinan Formation) overlain by Paleozoic to Mesozoic clastic supracrustal rocks (JBGMR, 1988, 2007). Phanerozoic granitoids with predominantly Mesozoic ages are widespread in the region, although a few Permian plutons also occur (JBGMR, 1988, 2007; Zhang et al., 2004; Wu et al., 2011). In addition to the granitoids, a few small mafic intrusions crop out in the region (Fig. 1b). The five Mesozoic plutons selected for this study are the Donggou, Tazigou, Shangtan, Yinxing, and Shangnan plutons.

2.1. Donggou pluton (14JEW2)

The Donggou pluton (43°10′53″N, 129°9′13″E) is located near Donggou village about 52 km southwest of Wangqing County (Fig. 1b). It consists of granodiorite with a medium–coarse granular granitic texture and a massive structure (Fig. 2a). The main minerals are quartz (~22%), plagioclase (~55%), alkali feldspar (~9%), hornblende (~7%), and biotite (~6%), with accessory magnetite, apatite, and zircon.

2.2. Tazigou pluton (14JEW3)

Located near Tazigou village, about 28 km northeast of Wangqing town (Fig. 1b), the Tazigou pluton (43°25′2″N, 130°5′1″E) consists of monzogranite with a medium–coarse granular granitic texture and a massive structure (Fig. 2b). The main minerals are quartz (~25%), plagioclase (~34%), alkali feldspar (~36%), and biotite (~4%), with accessory apatite and zircon.

2.3. Shangtan pluton (14JEW8)

Located near Shangtan village, about 40 km south of Tumen city (Fig. 1b), the Shangtan pluton (42°37′3″N, 129°46′25″E) consists of diorite with a medium–coarse granular texture and a massive structure (Fig. 2c and d). The main minerals are plagioclase (~65%), alkali feldspar (~5%), hornblende (~14%), clinopyroxene (~6%), biotite (~6%), and minor quartz (~3%). The accessory minerals are magnetite, apatite, and zircon.

2.4. Yinxing pluton (14JEW11)

Located near Yinxing village, about 13 km northeast of Helong city (Fig. 1b), the Yinxing pluton (42°38′18″N, 129°5′55″E) consists of gabbro–diorite with a fine–medium granular texture and a massive structure (Fig. 2e). The main minerals are plagioclase (~62%), hornblende (~20%), clinopyroxene (~8%), biotite (~7%), and minor

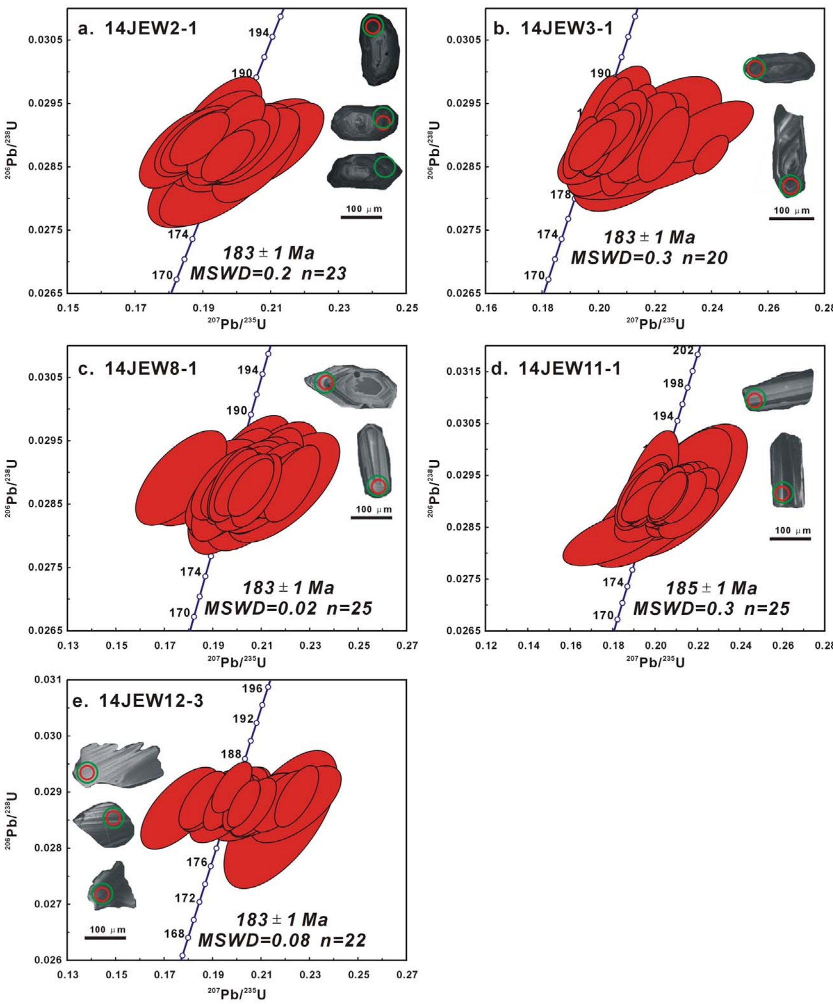

Fig. 3. Cathodoluminescence (CL) images of selected zircons and zircon U–Pb concordia diagrams for the Early Jurassic igneous rocks in this study. Red and green circles on zircons show the location of U-Pb analyses (spot size of 31 μm) and the Hf analyses (spot size of 44 μm), respectively. (For interpretation of the references to colour in this figure legend, the reader is referred to the web version of this article.)

quartz (~2%). The accessory minerals are magnetite, apatite, and zircon.

2.5. Shangnan pluton (14JEW12)

The Shangnan pluton is composed of gabbro–diorite. It was previously mapped as late Permian (JBGMR, 2007) at a site (42°35′15″N, 129°3′54″E) near Shangnan village in Helong City (Fig. 1g). Our samples are coarse-grained and massive, and contain plagioclase (~62%), hornblende (~20%), clinopyroxene (~8%), biotite (~8%), minor quartz (~2%), and accessory magnetite, apatite, and zircon (Fig. 2f).

3. Analytical methods

3.1. Zircon U–Pb dating

Zircons were separated from the samples using conventional crushing, heavy liquid, and magnetic separation techniques before the separates were purified by handpicking under a binocular microscope at the Langfang Yantuo Geological Service, Hebei Province, China. The handpicked zircons were mounted in epoxy resin and polished to expose grain centers. Using a combination of cathodoluminescence (CL) and optical microscopy, the clearest, least fractured rims of the zircon crystals were selected as suitable targets for laser ablation analyses. U–Pb dating was carried out using the LA–ICP–MS system at the CAS Key Laboratory of Mineralogy and Metallogeny, Guangzhou Institute of Geochemistry, Guangzhou, China. The system consists of an Agilent 7900 ICP–MS coupled with a Resonetics RESOlution S-155 laser. This laser ablation system is large (155 × 105 cm), and can load 20 sample mounts at a time. A Squid smoothing device was used to reduce statistical errors induced by the laser-ablation pulses, and to improve the quality of the data (Tu et al., 2011; Li et al., 2012). Helium gas carrying the ablated sample aerosol was mixed with argon carrier gas, together with nitrogen as an additional di-atomic gas to enhance sensitivity, before finally flowing into the ICP. Laser ablation was operated at a constant energy of 80 mJ and at 8 Hz, with a spot diameter of 31 μm. Element corrections were made for mass bias drift, which was evaluated by reference to standard glass NIST 610. Temora was used as the age standard ($^{206}Pb/^{238}U$ = 416.8 Ma). Trace-element concentrations were determined by normalizing count rates for each analyzed element to those for Si, and assuming SiO_2 to be stoichiometric in zircon (Tu et al., 2011; Li et al., 2012). The ICPMSDataCal (Ver. 9.6; Liu et al., 2008, 2010) and Isoplot (Ver. 3.0; Ludwig, 2003) programs were used for data reduction, and common Pb corrections were undertaken following Anderson (2002). The uncertainties on individual LA–ICP–MS analyses are quoted at the 1σ level, and errors on weighted mean ages are quoted at the 95% (2σ) confidence level. All the dating results are presented in Table 1.

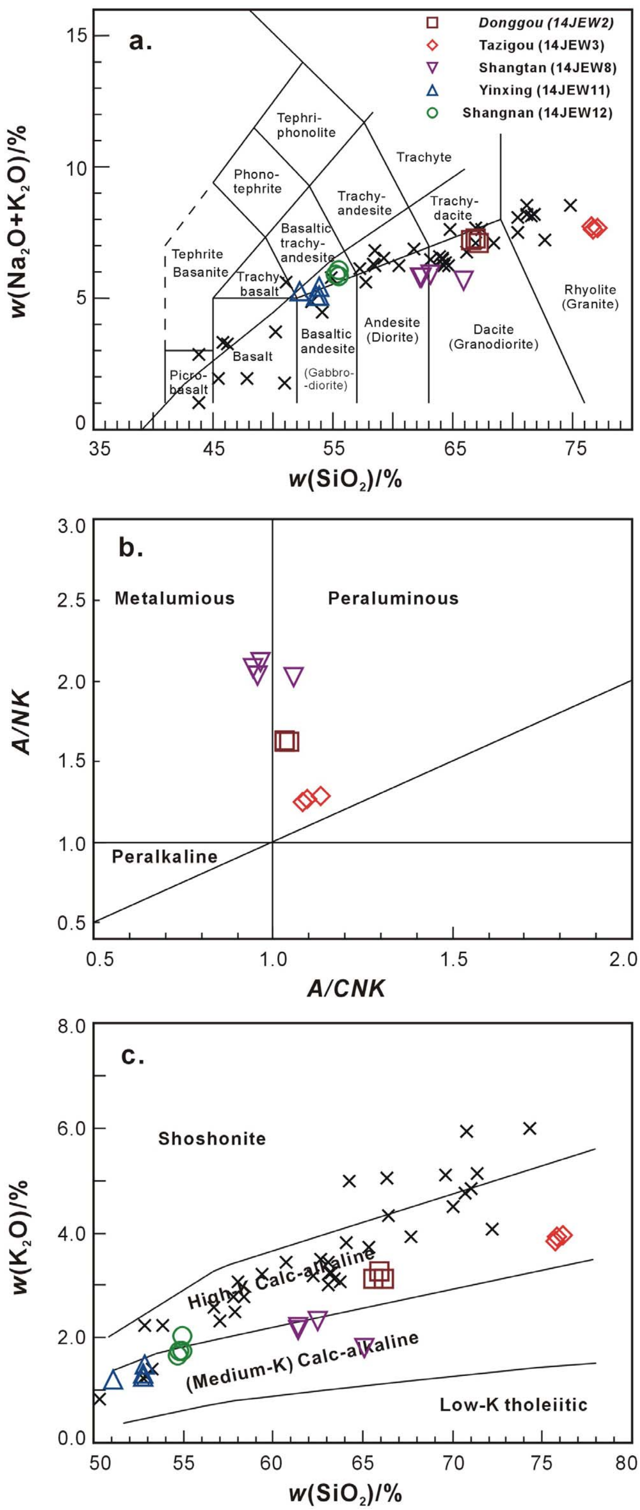

Fig. 4. (a) Plot of total alkali versus SiO_2 (TAS), (b) A/NK versus A/CNK, and (c) K_2O versus SiO_2. The boundary lines are from Irvine and Baragar (1971), Peccerillo and Taylor (1976), Maniar and Piccoli (1989), respectively. The symbols are the same as those in (a). Symbol of × shows the coeval calc-alkaline igneous rocks in the study area (data from Wu et al., 2013; He et al., 2014; Lei et al., 2014; Zhang et al., 2014; Guo et al., 2015; Liu et al., 2015).

3.2. Major and trace element analyses

Samples for whole-rock analysis were cleaned, and altered material removed, prior to crushing in an agate mill to pass ~200 mesh. The whole-rock major and trace element abundances were obtained at the

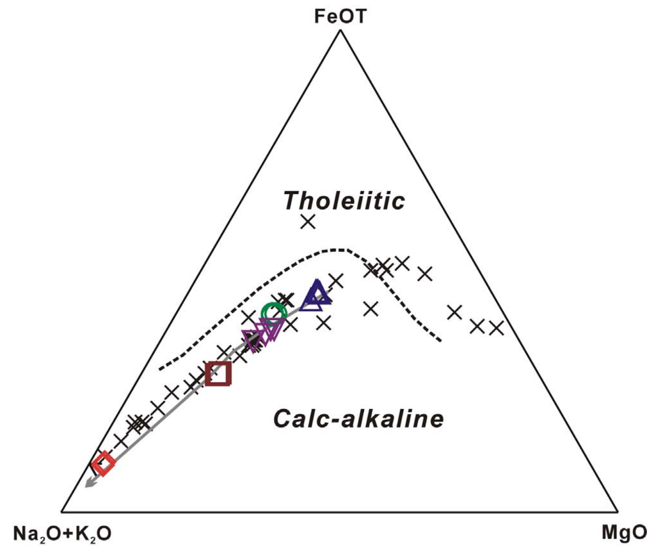

Fig. 5. AFM (total alkalis-FeOT-MgO) diagram for the Early Jurassic intrusive rocks in this study. The continuous discrimination line between Calc-alkaline and Tholeiitic series is from Irvine and Baragar (1971). The symbols are the same as those in Fig. 4a.

State Key Laboratory of Geological Processes and Mineral Resources, China University of Geosciences, Wuhan, China. Major elements were analyzed by X-ray fluorescence (XRF) using a Rigaku RIX 2100 spectrometer. Trace elements were determined by ICP–MS after acid digestion of samples in Teflon bombs using an Agilent 7500a equipped with a shield torch. Analytical uncertainties are between 1% and 3%, and analyses of the BHVO-1 (basalt), BCR-2 (basalt), and AGV-1 (andesite) standards indicate that the analytical precision for major elements was better than 5% and for trace elements generally better than 10% (Rudnick et al., 2004). Table 2 presents the major and trace element compositions of the Early Jurassic rocks analyzed in this study.

3.3. Hf isotope analyses

In situ zircon Hf isotope analyses were undertaken by MC–ICP–MS (Neptune Plus) equipped with a 193 nm ArF excimer laser ablation system at the State Key Laboratory of Geological Processes and Mineral Resources, China University of Geosciences. A simple Y junction downstream from the sample cell was used to add small amounts of nitrogen (4 ml min^{-1}) to the argon gas (Hu et al., 2008); the addition of nitrogen in combination with the use of a newly designed X skimmer and Jet sample cones within the Neptune Plus instrument improved the signal intensities of Hf, Yb, and Lu by factors of 5.3, 4.0, and 2.4, respectively, when compared with standard arrangements. All data were acquired using a single spot ablation mode and a 44 µm spot size. Each measurement consisted of 20 s of background signal acquisition followed by 50 s of ablation signal acquisition. Details of the operating conditions for the laser ablation system and the MC–ICP–MS instrument, and details of the analytical methods used during this study, are given in Hu et al. (2012a, 2012b). The zircon Hf isotope analyses are presented in Table 3.

4. Analytical results

4.1. Zircon U–Pb dating

Zircons separated from granodiorite (sample 14JEW2-1) are subhedral to euhedral and display fine-scale oscillatory zoning in CL images (Fig. 3a). These properties, combined with Th/U ratios of 0.36–0.67, are indicative of a magmatic origin (Pupin, 1980; Koschek, 1993). The $^{206}Pb/^{238}U$ ages of 23 analyzed spots on these zircons range from 180 to 185 Ma, yielding a weighted mean

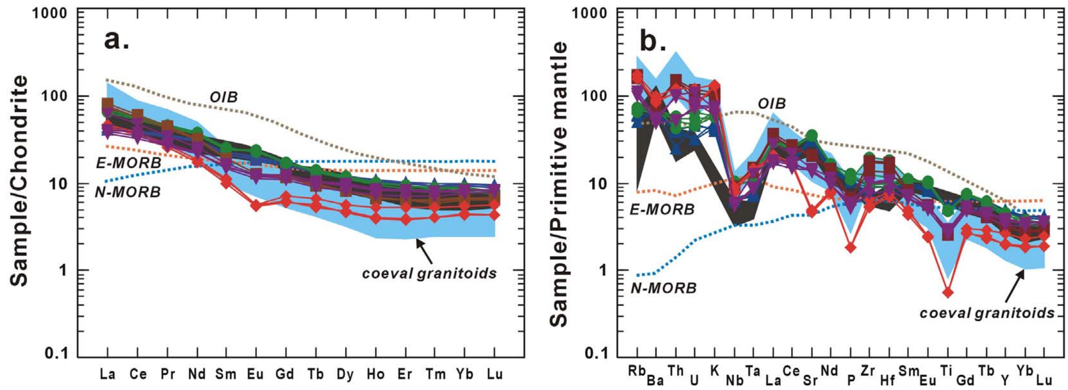

Fig. 6. (a) Chondrite-normalized REE patterns, and (b) primitive mantle-normalized trace element spidergrams for the Early Jurassic intrusive rocks in this study. Chondrite and primitive-mantle values are from Boynton (1984) and Sun and McDonough (1989), respectively. The symbols are the same as those in Fig. 4a. The shaded areas are from Wilson (1989). The values of OIB, E-MORB, and N-MORB are from Sun and McDonough (1989).

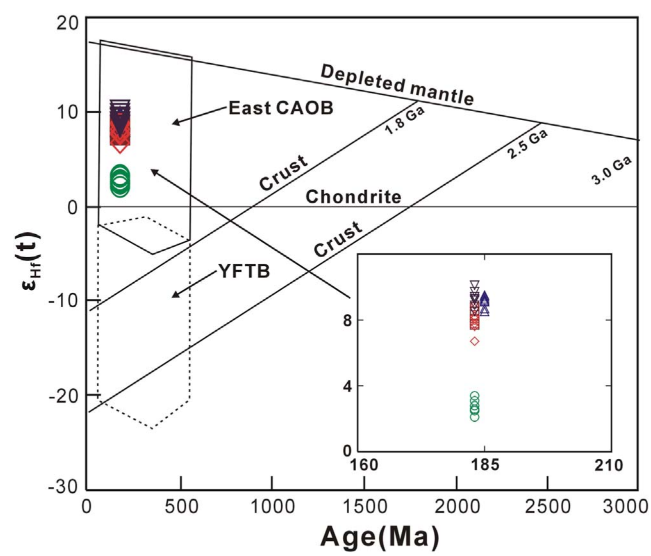

Fig. 7. $\varepsilon_{Hf}(t)$ versus U-Pb ages of zircons from the Early Jurassic igneous rocks in this study. CAOB – the Central Asian Orogenic Belt and YFTB – the Yanshan Fold and Thrust Belt (Yang et al., 2006). The symbols are the same as those in Fig. 4a.

$^{206}Pb/^{238}U$ age of 183 ± 1 Ma (MSWD = 0.2; Fig. 3a).

Zircons from a monzogranite (sample 14JEW3-1) in the Tazigou pluton (Fig. 1b) are also magmatic, as evidenced by the presence of oscillatory growth zoning (Fig. 3b) and high Th/U ratios (0.23–1.39; Table 1). The $^{206}Pb/^{238}U$ ages from 20 zircon analyses range from 181 to 185 Ma, yielding a weighted mean $^{206}Pb/^{238}U$ age of 183 ± 1 Ma (MSWD = 0.3; Fig. 3b).

Zircons separated from diorite (sample 14JEW8-1) in the Shangtan pluton (Fig. 1b) are euhedral, show fine-scale oscillatory zoning in CL images (Fig. 3c), and have Th/U ratios of 0.39–0.83, consistent with a magmatic origin (Pupin, 1980; Koschek, 1993). The $^{206}Pb/^{238}U$ ages from 25 analyses of zircons vary from 182 to 184 Ma, yielding a weighted mean $^{206}Pb/^{238}U$ age of 183 ± 1 Ma (MSWD = 0.02; Fig. 3c).

Zircons from gabbro–diorite (sample 14JEW11-1) in the Yinxing pluton (Fig. 1b) are euhedral to subhedral, display clear striped absorption patterns in CL images (Fig. 3d), and yield Th/U ratios of 0.29–0.94, indicating a magmatic origin. The $^{206}Pb/^{238}U$ ages from 25 analyses of zircons range from 180 to 186 Ma, yielding a weighted mean $^{206}Pb/^{238}U$ age of 185 ± 1 Ma (MSWD = 0.3; Fig. 3d).

Zircons from sample 14JEW12-3, a gabbro–diorite from the Shangnan pluton (Fig. 1b), are euhedral or subhedral, show striped absorption bands in CL images (Fig. 3e), and yield Th/U ratios of 0.33–1.36, again indicating a magmatic origin (Pupin, 1980; Koschek, 1993). The $^{206}Pb/^{238}U$ ages from 22 analyses of zircons range from 181 to 185 Ma, yielding a weighted mean $^{206}Pb/^{238}U$ age of 183 ± 1 Ma (MSWD = 0.08; Fig. 3e).

In summary, the zircons analyzed in present study are magmatic in origin and the weighted mean $^{206}Pb/^{238}U$ ages of the zircons therefore represent zircon crystallization ages. These results are in turn interpreted as the emplacement ages of the sampled plutons (183–185 Ma; Fig. 3).

4.2. Geochemistry

4.2.1. Major and trace elements

The loss on ignition (LOI) during sample analysis was low (Table 2: 0.58–1.52) and the Early Jurassic intrusive rocks show SiO_2 contents from 51.1 to 76.1 wt.%, Na_2O contents from 3.51 to 4.09 wt.%, and K_2O contents from 1.20 to 3.96 wt.%. The rocks plot in the fields of gabbro–diorite, diorite, granodiorite, and granite on the total alkalis versus SiO_2 diagram (TAS diagram; Fig. 4a).

The mafic rocks have SiO_2 concentrations of 51.11–54.96 wt.%, TiO_2 concentrations of 1.02–1.20 wt.%, Al_2O_3 concentrations of 19.0–20.2 wt.%, TFe_2O_3 concentrations of 6.38–8.39 wt.%, MgO concentrations of 2.42–3.93 wt.%, and Mg# values of 43–48. The felsic rocks have SiO_2 concentrations of 61.4–76.1 wt.%, TFe_2O_3 concentrations of 0.95–5.61 wt.%, MgO concentrations of 0.23–2.55 wt.%, CaO concentrations of 0.85–5.40 wt.%, and A/CNK [molar Al_2O_3/(CaO + Na_2O + K_2O)] values of 0.95–1.13, indicating that they are transitional between metaluminous and peraluminous on the A/NK versus A/CNK diagram (Fig. 4b). On the SiO_2 versus K_2O diagram, the Early Jurassic intrusive rocks plot mostly along the boundary between the medium-K and high-K calc-alkaline series (Fig. 4c), defining a calc-alkaline evolutionary trend (Fig. 5).

The Early Jurassic mafic rocks (Yinxing and Shangnan plutons) have slightly variable concentrations of light rare earth elements (LREE) (70.5–102 ppm), Th (2.14–5.04 ppm), and U (0.66–1.35 ppm) (Table 2; Fig. 6). Their $(La/Yb)_N$ and δEu values range from 4.58 to 8.81 and from 1.01 to 1.16, respectively (Fig. 6a). In addition, these mafic rocks are characterized by LREE and large ion lithophile element (LILE) enrichments, and heavy rare earth element (HREE) and high field strength element (HFSE; e.g., Nb, Ta, and Ti) depletions, distinct from OIB (ocean island basalt) and MORB (mid-ocean ridge basalt), but similar to subduction-related magmas (Fig. 6b).

Compared with the Early Jurassic mafic rocks, the dioritic plutons (Donggou and Shangtan) have higher LREE (7.4–103.9 ppm) and lower HREE abundances (9.62–11.56 ppm), and show negative Eu anomalies (δEu = 0.84–0.94; Fig. 6a). In addition, when compared with the other samples in the present study, the Tazigou monzogranites (14JEW3) have the lowest REE abundances (63.8–69.1 ppm), strong negative Eu anomalies (δEu = 0.62–0.69), and depletions in Sr, P, and Ti

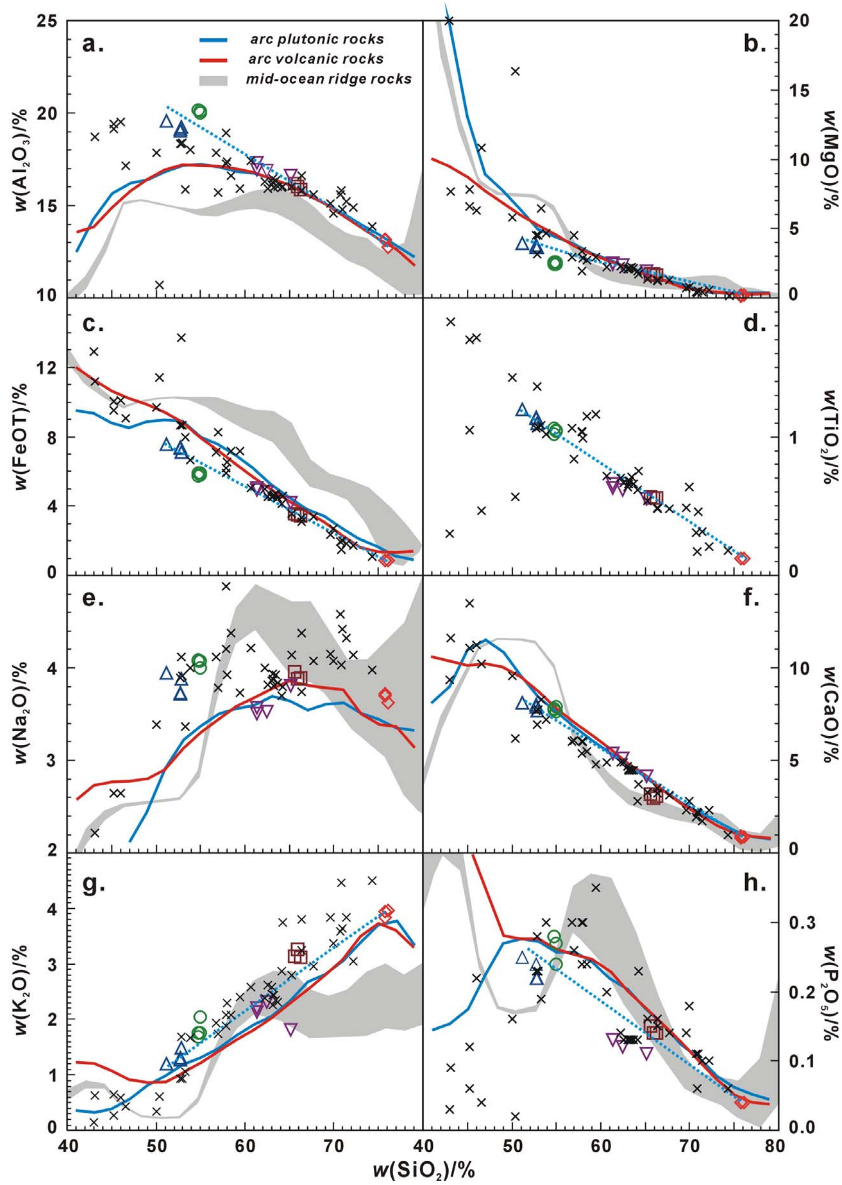

Fig. 8. Major-element Harker diagrams. The symbols are the same as those in Fig. 4a. The red, blue curves, and shaded areas are from Keller et al. (2015). (For interpretation of the references to colour in this figure legend, the reader is referred to the web version of this article.)

(Fig. 6a and b).

4.2.2. In situ zircon Hf isotope compositions

Some of the analysis sites for zircon U–Pb dating were also used for *in situ* zircon Hf isotope analyses (Table 3). The zircons from the Early Jurassic mafic rocks of the Yinxing and Shangnan plutons have slightly different Hf isotope compositions (Fig. 7). Zircons from the Yinxing gabbro–diorite (14JEW11-1) have $^{176}Hf/^{177}Hf$ ratios that vary from 0.282905 to 0.282931, corresponding to $\varepsilon_{Hf}(t)$ values and Hf single-stage (T_{DM1}) ages of +8.5 to +9.5 and 464–505 Ma, respectively (Table 3). In contrast, zircons from the Shangnan gabbro–diorite (14JEW12-3) have low $^{176}Hf/^{177}Hf$ ratios (0.282725–0.282763), and their $\varepsilon_{Hf}(t)$ values and Hf single-stage (T_{DM1}) ages range from +2.1 to +3.4 and 709 to 774 Ma, respectively (Table 3).

The zircons from the dioritic rocks of the Donggou and Shangtan plutons have similar Hf isotope compositions (Fig. 7), with $^{176}Hf/^{177}Hf$ ratios of 0.282881–0.282946 and $\varepsilon_{Hf}(t)$ values of +7.8 to +10.1 (Table 3). In addition, zircons from the Tazigou monzogranite have $^{176}Hf/^{177}Hf$ ratios of 0.282855–0.282917, corresponding to $\varepsilon_{Hf}(t)$ values and two-stage (T_{DM2}) Hf model ages of +6.7 to +8.9 and 597–718 Ma, respectively (Table 3).

5. Discussion

5.1. Early Jurassic magmatism in the eastern part of NE China

NE China is characterized by immense volumes of granitoids that were traditionally considered to have formed mainly during the Paleozoic or early Mesozoic, a view that was based on unreliable isotopic age data (JBGMR, 1988; HBGMR, 1993). In the past decade, precise geochronological analyses (e.g., Wu et al., 2011) have shown that most of the granitoids in the region were emplaced during the Mesozoic (Fig. 1b). However, there are still competing views on the Mesozoic tectonics of NE China, especially with regard to the eastern part of the region (Wu et al., 2011). Furthermore, few studies have examined the geochronology and petrogenesis of mafic intrusions in NE China, simply because these rocks are sparse and small in volume when compared with the granitoids (Yu et al., 2012; Guo et al., 2015; Wang et al., 2015).

The available geochronological data of early Mesozoic magmatism

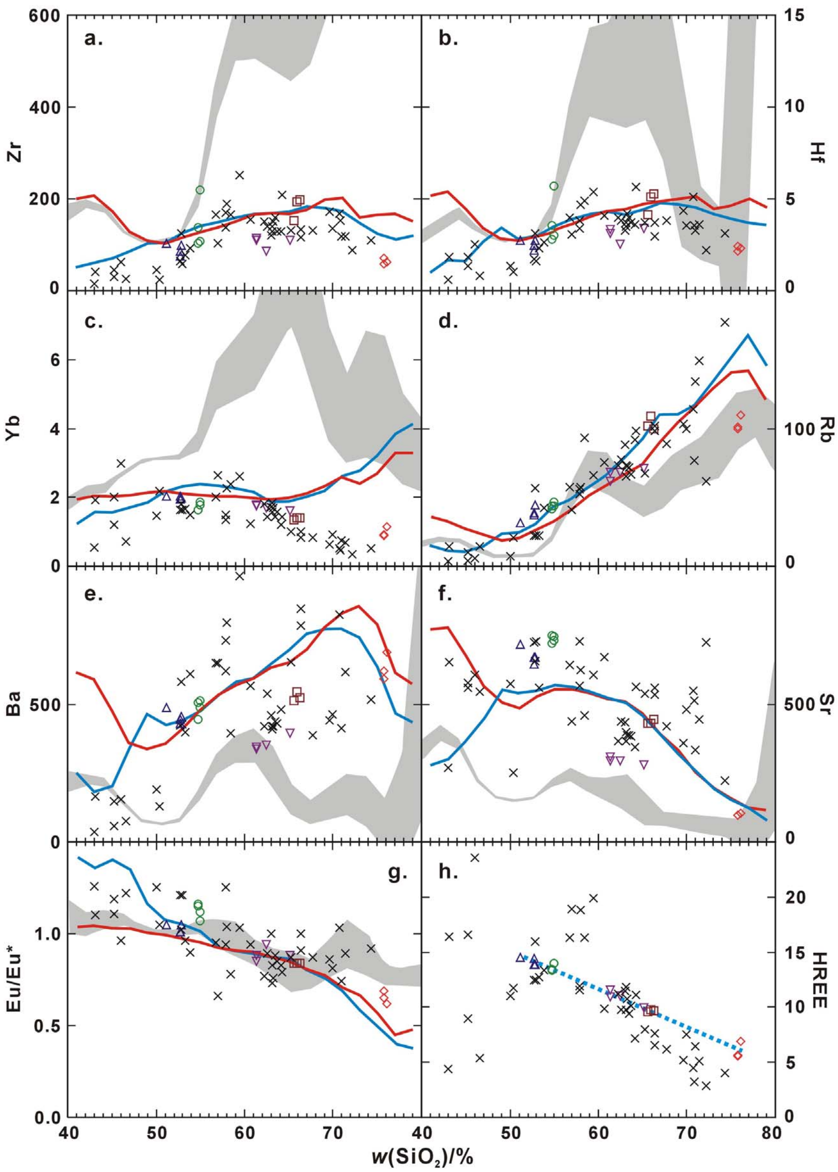

Fig. 9. Trace-element Harker diagrams. The symbols are the same as those in Fig. 4a. The red, blue curves, and shaded areas are from Keller et al. (2015). (For interpretation of the references to colour in this figure legend, the reader is referred to the web version of this article.)

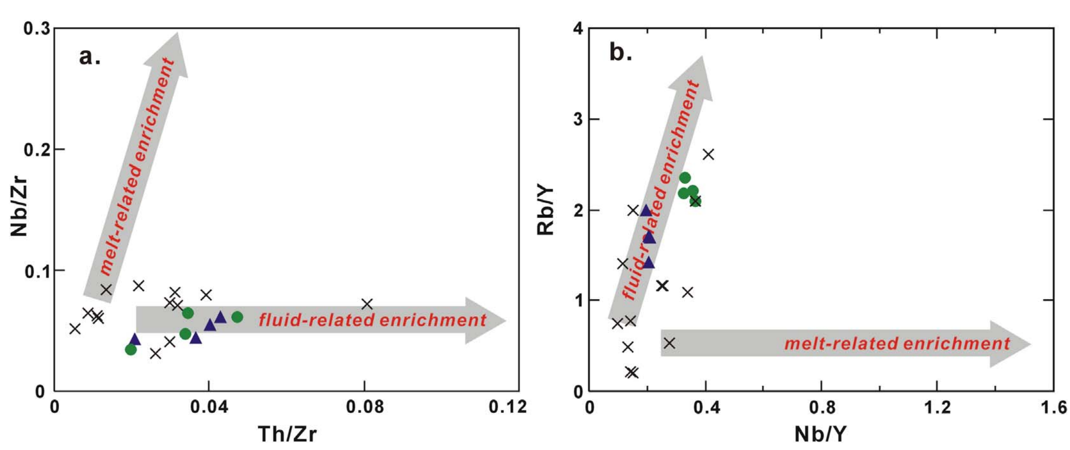

Fig. 10. (a) Th/Zr versus Nb/Zr (Kepezhinskas et al., 1997), (b) Rb/Y versus Nb/Y (Kepezhinskas et al., 1997), The symbols are the same as those in Fig. 4a.

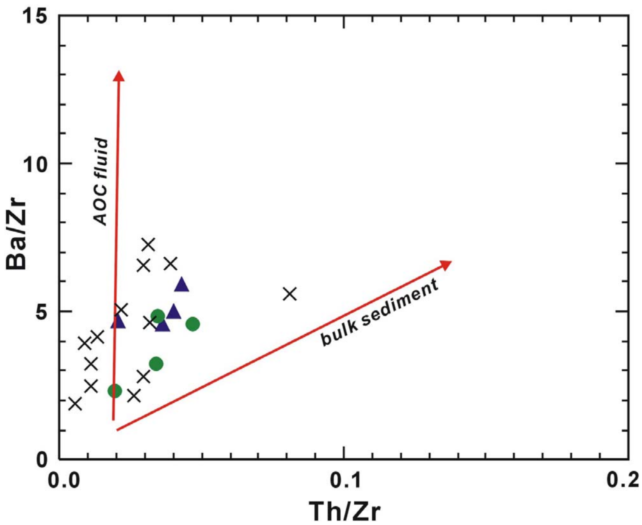

Fig. 11. Plots of Ba/Zr versus Th/Zr (Ishuzuka et al., 2003). The symbols are the same as those in Fig. 4a.

in the eastern part of NE China form two main groups: one in the Late Triassic and one in the Early Jurassic (Xu et al., 2009, 2013a, 2013b; Wu et al., 2011). Many studies have focused on the geochronological framework of the widespread Mesozoic granitoids, as well as the tectonic setting of the Late Triassic magmatism (Xu et al., 2009; Wang et al., 2015). Comparatively few studies have considered the Early Jurassic igneous rocks (Xu et al., 2013a, 2013b; Guo et al., 2015), which are key to revealing the subduction history of the Paleo-Pacific Plate beneath the Eurasian continent. Two relevant issues need to be addressed: (1) the scale and (2) the rock associations of the Early Jurassic magmatism in NE China.

The dating results presented in this study provide clear evidence for an Early Jurassic magmatic event (183–185 Ma; Fig. 3) in the eastern part of NE China. The existence of this event is supported by other independent studies (Wu et al., 2011, 2013; Xu et al., 2013a, 2013b; He et al., 2014; Lei et al., 2014; Zhang et al., 2014; Guo et al., 2015; Liu et al., 2015) that show widespread Early Jurassic volcanic and/or intrusive rocks in several of the massifs of NE China (Wu et al., 2011), particularly in the eastern parts of Jilin and Heilongjiang provinces (Xu et al., 2013a, 2013b; Guo et al., 2015), and in the Lesser Xing'an Range (Yu et al., 2012). These data delineate a NE-trending Early Jurassic

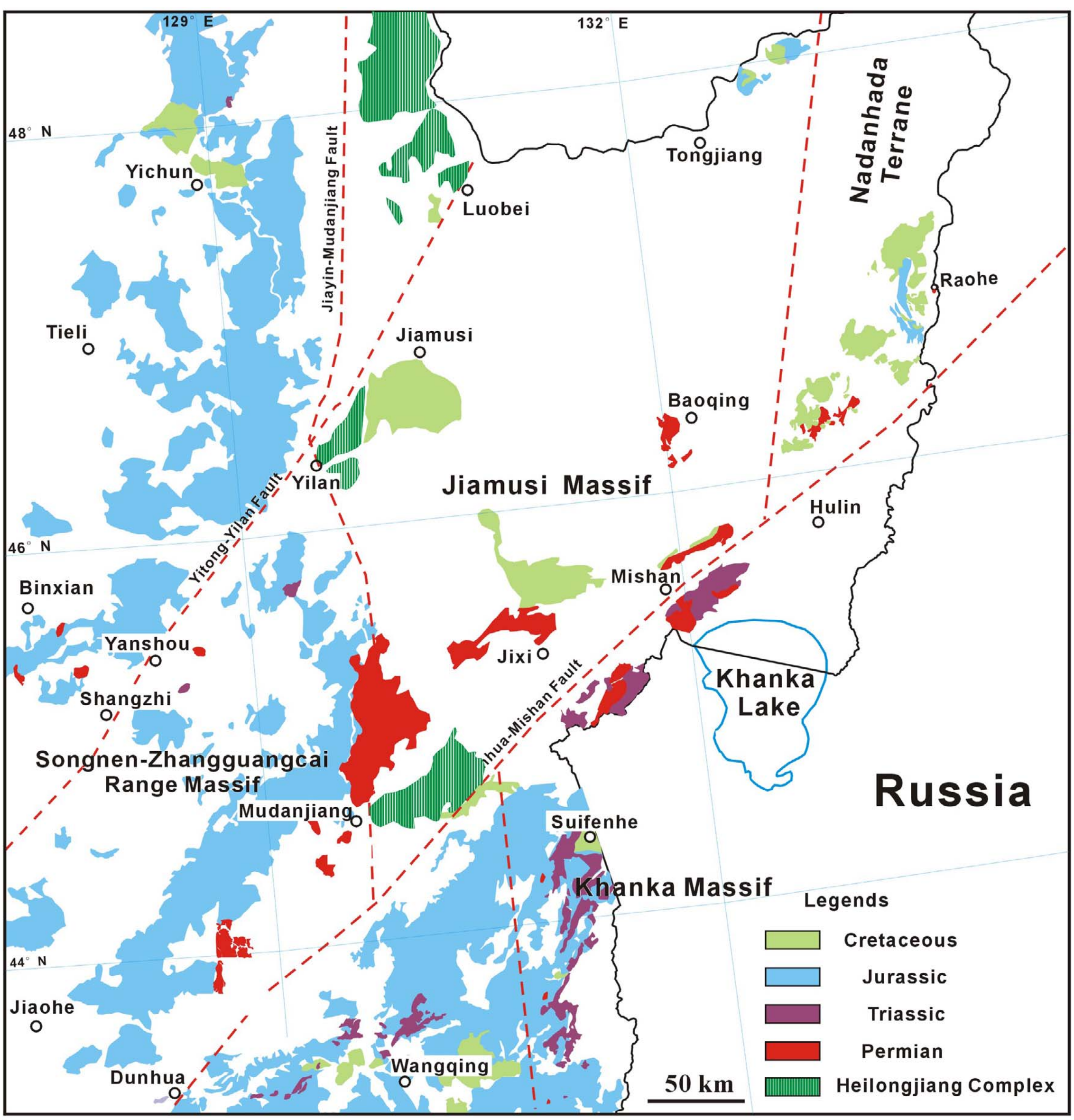

Fig. 12. The distribution map of Permian-Cretaceous igneous rocks in eastern of Heilongjiang and Jilin provinces of NE China (modified after Wu et al., 2011; Xu et al., 2013a, 2013b; Wang et al., 2016).

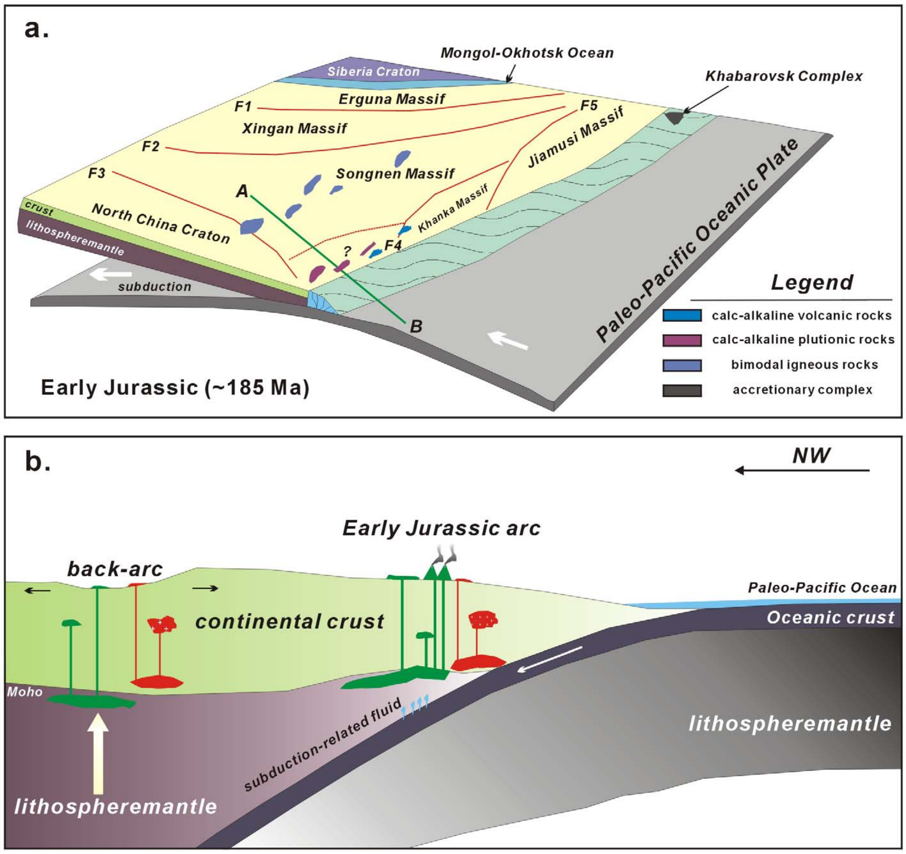

Fig. 13. (a) Cartoon illustrations showing a tectonic evolutional model for the subduction initiation of the Paleo-Pacific Plate in NE China. (b) Suppositional profile across the eastern part of NE China, its location marked as green line A-B in (a). (For interpretation of the references to colour in this figure legend, the reader is referred to the web version of this article.)

magmatic belt within the eastern margin of Eurasia (Fig. 12), in which a wide variety of igneous rocks, from ultramafic to felsic, were emplaced.

5.2. Petrogenesis of the Early Jurassic igneous rocks

5.2.1. Diversity of Early Jurassic calc-alkaline intrusions: magmatic differentiation or mixing?

A wide variety of Early Jurassic igneous rock types coexist in the present study area and adjacent regions (Fig. 1). The effects of alteration need to be evaluated before a petrogenetic assessment of these rocks is undertaken. The low LOI values documented above (Table 2: 0.50–1.52) suggest that the rocks in this study are fresh and have not undergone significant secondary alteration. Furthermore, HFSEs are generally considered immobile during alteration or weathering (Polat et al., 2002; Wu et al., 2007a, 2007b), and the behavior of these elements can be used to trace the primary magmatic features regardless of any alteration or weathering.

To understand the petrogenesis of the Early Jurassic igneous rocks, it is crucial that the presence or absence of any genetic relationships among them (e.g., fractional crystallization or magma mixing) be established. The Jurassic igneous appear to define a common magmatic suite with coherent variations in their major and trace elements (Figs. 8 and 9). It seems, therefore, that fractional crystallization is a possible mechanism for explaining the diversity of the Early Jurassic calc-alkaline intrusions. Recently, Keller et al. (2015) applied computational statistical techniques to a data set of major and trace element geochemical analyses for more than 290,000 continental igneous rock samples, and they concluded that fractional crystallization was the dominant mechanism for producing intermediate and felsic magmas in arc settings. Major and trace elements from magmatic rocks in arc-type tectonic settings follow curvilinear differentiation trends (red and blue lines in Figs. 8 and 9). Plotted against SiO_2, the majors and trace element concentrations of the samples described here follow curvilinear differentiation trends that fall close to the arc data set, and the trends are similar to the variations shown by plutonic rocks in other arc settings (Figs. 8 and 9; Keller et al., 2015). Therefore, the decreases in Al_2O_3, MgO, TiO_2, CaO, P_2O_5, and Sr, and the increases in K_2O and Rb with increasing silica (Figs. 8 and 9) could be related to the combined fractionation of plagioclase, hornblende, apatite, and titanite. The obvious decrease in FeO_T content with increasing SiO_2 (Fig. 8c) could be related to the removal of hornblende rich in Fe relative to Mg in an intermediate–acidic magma. Fractional crystallization is also consistent with the negative correlation between HREE contents and SiO_2 (Fig. 9h; Table 2). Remarkably, the Shangnan Pluton (gabbro–diorite) has lower Mg# values and compatible element concentrations than the Donggou Pluton (granodiorite), implying that magmatic mixing or crustal assimilation occurred during magmatic differentiation. The above scenario is supported by the varied $\varepsilon_{Hf}(t)$ values in the gabbro–diorite Shangnan and Yinxing plutons (Fig. 7). The region is located at the junction of the CAOB and the northeastern margin of the NCC, and magmatic mixing can result in similar Hf isotopic compositions within a single pluton (Yang et al., 2007). It is therefore conceivable that small-scale intra-pluton magma mixing occurs, but its effect on the compositions of basic and felsic end-members of a related suite of igneous rocks is probably insignificant. For the purposes of this discussion, we assume that magmatic mixing had minimal influence on the compositions of the Early Jurassic igneous rocks.

Although crystal fractionation is a plausible mechanism for producing the Early Jurassic magmatic assemblage in the present study area, it does not seem likely, given the following observations and considerations that indicate all of the rocks were derived from fractionation of a single mafic parent magma. (1) The majority of the coeval igneous rocks in the present study area and adjacent regions are felsic rather than mafic (Fig. 1b; Wu et al., 2011; Xu et al., 2013a, 2013b; Guo et al.,

Table 1
Zircon U-Pb dating data for the Early Jurassic igneous rocks in eastern Jilin Province, NE China.

Sample no.	Th (ppm)	U (ppm)	Th/U	Isotopic ratios						Ages (Ma)					
				$^{207}Pb/^{206}Pb$		$^{207}Pb/^{235}U$		$^{206}Pb/^{238}U$		$^{207}Pb/^{206}Pb$		$^{207}Pb/^{235}U$		$^{206}Pb/^{238}U$	
				Ratio	1σ	Ratio	1σ	Ratio	1σ	Age	1σ	Age	1σ	Age	1σ
14JEW2-1 Donggou pluton (granodiorite)															
14JEW2-1-01	130	292	0.44	0.05141	0.00220	0.20487	0.00903	0.02883	0.00040	259	76	189	8	183	3
14JEW2-1-02	165	423	0.39	0.04863	0.00173	0.19505	0.00713	0.02897	0.00031	130	65	181	6	184	2
14JEW2-1-03	135	276	0.49	0.04665	0.00179	0.18731	0.00769	0.02891	0.00037	31	64	174	7	184	2
14JEW2-1-04	185	278	0.67	0.04973	0.00373	0.19415	0.01353	0.02843	0.00058	182	121	180	12	181	4
14JEW2-1-05	216	490	0.44	0.05087	0.00172	0.20261	0.00672	0.02887	0.00040	235	51	187	6	184	3
14JEW2-1-06	115	250	0.46	0.04723	0.00186	0.18880	0.00749	0.02891	0.00033	61	67	176	6	184	2
14JEW2-1-07	197	430	0.46	0.05036	0.00185	0.19996	0.00742	0.02883	0.00040	212	60	185	6	183	3
14JEW2-1-08	87.9	245	0.36	0.05112	0.00244	0.20604	0.01139	0.02887	0.00047	246	97	190	10	183	3
14JEW2-1-09	149	228	0.65	0.05298	0.00225	0.21133	0.00947	0.02885	0.00044	328	74	195	8	183	3
14JEW2-1-10	335	544	0.62	0.04972	0.00134	0.19983	0.00561	0.02916	0.00031	182	45	185	5	185	2
14JEW2-1-11	209	496	0.42	0.04731	0.00137	0.18898	0.00579	0.02895	0.00028	65	51	176	5	184	2
14JEW2-1-12	124	288	0.43	0.04911	0.00158	0.19483	0.00631	0.02881	0.00029	153	57	181	5	183	2
14JEW2-1-13	273	574	0.48	0.04988	0.00301	0.19424	0.01133	0.02824	0.00044	189	138	180	10	180	3
14JEW2-1-14	254	569	0.45	0.05075	0.00145	0.20124	0.00564	0.02881	0.00029	230	46	186	5	183	2
14JEW2-1-15	101	258	0.39	0.04948	0.00256	0.19364	0.00904	0.02906	0.00057	171	72	180	8	185	4
14JEW2-1-16	119	271	0.44	0.04824	0.00208	0.19379	0.00864	0.02910	0.00040	111	76	180	7	185	2
14JEW2-1-17	164	396	0.41	0.05012	0.00203	0.19832	0.00774	0.02876	0.00036	201	67	184	7	183	2
14JEW2-1-18	211	396	0.53	0.05032	0.00283	0.19998	0.01091	0.02881	0.00046	210	96	185	9	183	3
14JEW2-1-19	137	318	0.43	0.04593	0.00188	0.18311	0.00787	0.02879	0.00041	−6	63	171	7	183	3
14JEW2-1-20	193	492	0.39	0.04877	0.00143	0.19410	0.00582	0.02879	0.00030	137	51	180	5	183	2
14JEW2-1-21	118	286	0.41	0.05183	0.00200	0.20556	0.00854	0.02866	0.00047	278	65	190	7	182	3
14JEW2-1-22	288	624	0.46	0.04962	0.00124	0.19729	0.00517	0.02868	0.00027	177	43	183	4	182	2
14JEW2-1-23	103	280	0.37	0.04971	0.00201	0.19714	0.00774	0.02875	0.00035	181	69	183	7	183	2
14JEW3-1 Tazigou pluton (monzogranite)															
14JEW3-1-01	437	804	0.54	0.04977	0.00146	0.19772	0.00551	0.02885	0.00027	184	47	183	5	183	2
14JEW3-1-02	157	486	0.32	0.05948	0.00280	0.23830	0.01089	0.02906	0.00032	585	105	217	9	185	2
14JEW3-1-03	426	1285	0.33	0.04874	0.00100	0.19353	0.00409	0.02881	0.00032	135	29	180	3	183	2
14JEW3-1-04	1875	3819	0.49	0.06050	0.00096	0.23974	0.00410	0.02870	0.00020	622	25	218	3	182	1
14JEW3-1-05	143	259	0.55	0.05027	0.00235	0.20007	0.00965	0.02879	0.00037	208	88	185	8	183	2
14JEW3-1-06	132	274	0.48	0.05136	0.00262	0.20507	0.01087	0.02885	0.00053	257	88	189	9	183	3
14JEW3-1-07	378	818	0.46	0.05265	0.00143	0.21071	0.00678	0.02893	0.00058	314	38	194	6	184	4
14JEW3-1-08	1320	1496	0.88	0.04934	0.00142	0.19925	0.00576	0.02918	0.00050	164	37	184	5	185	3
14JEW3-1-09	461	1516	0.30	0.05032	0.00131	0.20354	0.00557	0.02916	0.00050	210	34	188	5	185	3
14JEW3-1-10	628	1279	0.49	0.05431	0.00194	0.21838	0.00884	0.02896	0.00047	384	62	201	7	184	3
14JEW3-1-11	533	943	0.56	0.05610	0.00150	0.22299	0.00601	0.02886	0.00039	456	36	204	5	183	2
14JEW3-1-12	618	506	1.22	0.05059	0.00155	0.20276	0.00646	0.02901	0.00026	222	57	187	5	184	2
14JEW3-1-13	379	272	1.39	0.05174	0.00212	0.20594	0.00860	0.02897	0.00041	274	70	190	7	184	3
14JEW3-1-14	326	1420	0.23	0.05123	0.00161	0.20599	0.00734	0.02908	0.00042	251	55	190	6	185	3
14JEW3-1-15	1299	1196	1.09	0.05179	0.00125	0.20678	0.00535	0.02895	0.00037	276	36	191	4	184	2
14JEW3-1-16	35.9	98.0	0.37	0.05505	0.00446	0.21711	0.01744	0.02887	0.00070	414	137	199	15	183	4
14JEW3-1-17	243	243	1.00	0.05102	0.00232	0.20444	0.00929	0.02917	0.00061	242	66	189	8	185	4
14JEW3-1-18	867	778	1.11	0.05388	0.00212	0.21513	0.00816	0.02897	0.00047	366	56	198	7	184	3
14JEW3-1-19	248	249	1.00	0.05537	0.00476	0.21771	0.01854	0.02851	0.00034	427	197	200	15	181	2
14JEW3-1-20	3561	3998	0.89	0.05021	0.00100	0.20063	0.00443	0.02894	0.00038	205	28	186	4	184	2
14JEW8-1 Shangtan pluton (diorite)															
14JEW8-1-01	45.5	106	0.43	0.05149	0.00294	0.20477	0.01164	0.02884	0.00048	263	100	189	10	183	3
14JEW8-1-02	59.1	123	0.48	0.05120	0.00306	0.20113	0.01174	0.02884	0.00044	250	106	186	10	183	3
14JEW8-1-03	106	251	0.42	0.05100	0.00203	0.20288	0.00813	0.02881	0.00032	241	72	188	7	183	2
14JEW8-1-04	61.5	148	0.42	0.05557	0.00234	0.22021	0.00904	0.02885	0.00037	435	69	202	8	183	2
14JEW8-1-05	152	226	0.67	0.04990	0.00230	0.19898	0.00923	0.02880	0.00034	190	86	184	8	183	2
14JEW8-1-06	61.6	128	0.48	0.05210	0.00345	0.20555	0.01318	0.02879	0.00044	290	119	190	11	183	3
14JEW8-1-07	56.6	104	0.55	0.05518	0.00366	0.21923	0.01531	0.02877	0.00057	419	121	201	13	183	4
14JEW8-1-08	382	621	0.62	0.04989	0.00167	0.19867	0.00681	0.02880	0.00038	190	55	184	6	183	2
14JEW8-1-09	92.8	238	0.39	0.04978	0.00287	0.19786	0.01204	0.02882	0.00058	185	102	183	10	183	4
14JEW8-1-10	82.5	174	0.47	0.05371	0.00238	0.21320	0.00951	0.02886	0.00041	359	75	196	8	183	3
14JEW8-1-11	208	251	0.83	0.05357	0.00312	0.21220	0.01224	0.02873	0.00045	353	102	195	10	183	3
14JEW8-1-12	91.0	215	0.42	0.05227	0.00260	0.20578	0.01005	0.02867	0.00039	297	87	190	8	182	2
14JEW8-1-13	87.4	144	0.61	0.05315	0.00260	0.21124	0.01061	0.02887	0.00055	335	79	195	9	183	3
14JEW8-1-14	38.9	75.2	0.52	0.04526	0.00348	0.17690	0.01249	0.02892	0.00049	−6	121	165	11	184	3
14JEW8-1-15	80.4	160	0.50	0.04696	0.00381	0.18684	0.01493	0.02885	0.00045	47	146	174	13	183	3
14JEW8-1-16	227	530	0.43	0.05191	0.00159	0.20566	0.00626	0.02877	0.00030	282	51	190	5	183	2
14JEW8-1-17	201	337	0.60	0.05631	0.00195	0.22268	0.00763	0.02883	0.00040	465	51	204	6	183	2
14JEW8-1-18	114	263	0.43	0.04981	0.00166	0.19754	0.00658	0.02882	0.00039	186	53	183	6	183	2
14JEW8-1-19	86.9	139	0.63	0.04943	0.00236	0.19453	0.00900	0.02882	0.00037	168	84	180	8	183	2
14JEW8-1-20	60.3	134	0.45	0.05081	0.00350	0.20119	0.01421	0.02881	0.00072	232	116	186	12	183	4
14JEW8-1-21	121	253	0.48	0.05228	0.00165	0.20801	0.00690	0.02872	0.00038	298	51	192	6	183	2
14JEW8-1-22	49.7	91.7	0.54	0.05345	0.00385	0.21028	0.01545	0.02879	0.00067	348	125	194	13	183	4
14JEW8-1-23	53.6	125	0.43	0.05101	0.00259	0.20152	0.00994	0.02880	0.00041	241	87	186	8	183	3

(continued on next page)

Table 1 *(continued)*

Sample no.	Th (ppm)	U (ppm)	Th/U	Isotopic ratios						Ages (Ma)					
				$^{207}Pb/^{206}Pb$		$^{207}Pb/^{235}U$		$^{206}Pb/^{238}U$		$^{207}Pb/^{206}Pb$		$^{207}Pb/^{235}U$		$^{206}Pb/^{238}U$	
				Ratio	1σ	Ratio	1σ	Ratio	1σ	Age	1σ	Age	1σ	Age	1σ
14JEW8-1-24	61.8	120	0.52	0.04960	0.00299	0.19544	0.01115	0.02872	0.00043	177	103	181	9	183	3
14JEW8-1-25	101	206	0.49	0.04970	0.00239	0.19485	0.00909	0.02865	0.00048	181	77	181	8	182	3
14JEW11-1 Yinxing pluton (gabbro-diorite)															
14JEW11-1-01	80.1	183	0.44	0.05297	0.00272	0.21058	0.00994	0.02905	0.00048	328	77	194	8	185	3
14JEW11-1-02	403	544	0.74	0.05215	0.00170	0.20953	0.00611	0.02916	0.00037	292	43	193	5	185	2
14JEW11-1-03	328	450	0.73	0.05127	0.00148	0.20621	0.00615	0.02908	0.00031	253	49	190	5	185	2
14JEW11-1-04	453	566	0.80	0.05093	0.00152	0.20499	0.00611	0.02913	0.00036	237	46	189	5	185	2
14JEW11-1-05	291	374	0.78	0.04841	0.00149	0.19463	0.00636	0.02914	0.00037	119	53	181	5	185	2
14JEW11-1-06	21.0	73.1	0.29	0.05356	0.00525	0.21384	0.01962	0.02922	0.00084	353	156	197	16	186	5
14JEW11-1-07	215	372	0.58	0.04797	0.00161	0.19171	0.00642	0.02908	0.00037	98	55	178	5	185	2
14JEW11-1-08	52.5	123	0.43	0.05045	0.00346	0.20109	0.01341	0.02891	0.00045	216	157	186	11	184	3
14JEW11-1-09	143	213	0.67	0.04858	0.00238	0.19463	0.00901	0.02918	0.00048	128	76	181	8	185	3
14JEW11-1-10	53.5	120	0.45	0.05324	0.00390	0.21334	0.01513	0.02934	0.00071	339	117	196	13	186	4
14JEW11-1-11	305	481	0.63	0.05102	0.00168	0.20461	0.00682	0.02910	0.00039	242	52	189	6	185	2
14JEW11-1-12	392	535	0.73	0.05147	0.00169	0.20725	0.00727	0.02911	0.00041	262	55	191	6	185	3
14JEW11-1-13	297	461	0.64	0.04905	0.00166	0.19643	0.00645	0.02912	0.00039	150	52	182	5	185	2
14JEW11-1-14	78.5	148	0.53	0.05004	0.00281	0.19659	0.00960	0.02920	0.00077	197	65	182	8	186	5
14JEW11-1-15	392	524	0.75	0.05305	0.00170	0.21376	0.00693	0.02909	0.00033	331	53	197	6	185	2
14JEW11-1-16	234	460	0.51	0.04640	0.00422	0.18116	0.01633	0.02832	0.00036	18	199	169	14	180	2
14JEW11-1-17	419	446	0.94	0.05226	0.00192	0.20978	0.00783	0.02911	0.00043	297	58	193	7	185	3
14JEW11-1-18	359	516	0.70	0.04899	0.00141	0.19735	0.00604	0.02913	0.00041	148	45	183	5	185	3
14JEW11-1-19	264	416	0.63	0.05122	0.00155	0.20580	0.00603	0.02912	0.00030	251	48	190	5	185	2
14JEW11-1-20	234	379	0.62	0.05330	0.00192	0.21659	0.00901	0.02911	0.00036	342	72	199	8	185	2
14JEW11-1-21	183	351	0.52	0.04989	0.00484	0.19728	0.01866	0.02868	0.00062	190	221	183	16	182	4
14JEW11-1-22	583	713	0.82	0.04861	0.00185	0.19518	0.00728	0.02900	0.00026	129	70	181	6	184	2
14JEW11-1-23	590	666	0.89	0.05181	0.00180	0.20828	0.00702	0.02906	0.00033	277	56	192	6	185	2
14JEW11-1-24	275	437	0.63	0.05445	0.00257	0.21571	0.00927	0.02878	0.00032	390	77	198	8	183	2
14JEW11-1-25	178	330	0.54	0.05214	0.00194	0.20934	0.00767	0.02904	0.00033	292	63	193	6	185	2
14JEW12-3 Shangnan pluton (gabbro-diorite)															
14JEW12-3-01	140	185	0.75	0.04987	0.00257	0.19839	0.01026	0.02883	0.00041	189	93	184	9	183	3
14JEW12-3-02	4541	3347	1.36	0.05023	0.00089	0.20027	0.00420	0.02883	0.00034	205	28	185	4	183	2
14JEW12-3-03	448	419	1.07	0.04990	0.00193	0.19820	0.00753	0.02879	0.00028	190	70	184	6	183	2
14JEW12-3-04	1668	1223	1.36	0.05099	0.00112	0.20267	0.00449	0.02880	0.00028	240	33	187	4	183	2
14JEW12-3-05	2717	2435	1.12	0.05589	0.00120	0.22458	0.00602	0.02893	0.00036	448	37	206	5	184	2
14JEW12-3-06	124	373	0.33	0.05225	0.00164	0.20674	0.00630	0.02874	0.00034	297	48	191	5	183	2
14JEW12-3-07	76.9	115	0.67	0.05702	0.00330	0.22435	0.01242	0.02879	0.00045	492	95	206	10	183	3
14JEW12-3-08	114	150	0.76	0.05574	0.00414	0.21800	0.01548	0.02852	0.00081	442	107	200	13	181	5

(continued on next page)

Table 1 *(continued)*

Sample no.	Th (ppm)	U (ppm)	Th/U	Isotopic ratios						Ages (Ma)					
				$^{207}Pb/^{206}Pb$		$^{207}Pb/^{235}U$		$^{206}Pb/^{238}U$		$^{207}Pb/^{206}Pb$		$^{207}Pb/^{235}U$		$^{206}Pb/^{238}U$	
				Ratio	1σ	Ratio	1σ	Ratio	1σ	Age	1σ	Age	1σ	Age	1σ
14JEW12-3-09	268	313	0.86	0.05238	0.00301	0.20802	0.01212	0.02874	0.00040	302	108	192	10	183	3
14JEW12-3-10	333	383	0.87	0.04649	0.00159	0.18574	0.00654	0.02886	0.00034	23	53	173	6	183	2
14JEW12-3-11	684	737	0.93	0.04918	0.00130	0.19777	0.00545	0.02909	0.00030	156	45	183	5	185	2
14JEW12-3-12	196	244	0.80	0.05288	0.00208	0.20911	0.00821	0.02875	0.00036	324	66	193	7	183	2
14JEW12-3-13	246	285	0.86	0.04967	0.00252	0.19738	0.01000	0.02883	0.00041	180	91	183	8	183	3
14JEW12-3-14	424	406	1.04	0.05441	0.00180	0.21794	0.00800	0.02884	0.00036	388	60	200	7	183	2
14JEW12-3-15	144	192	0.75	0.04742	0.00187	0.18733	0.00705	0.02882	0.00034	70	62	174	6	183	2
14JEW12-3-16	212	250	0.85	0.05333	0.00225	0.21066	0.00881	0.02884	0.00033	343	74	194	7	183	2
14JEW12-3-17	298	375	0.79	0.04817	0.00205	0.19118	0.00770	0.02889	0.00034	108	70	178	7	184	2
14JEW12-3-18	178	220	0.81	0.04949	0.00249	0.19509	0.00972	0.02871	0.00040	171	89	181	8	182	3
14JEW12-3-19	146	177	0.83	0.04528	0.00297	0.17636	0.01075	0.02872	0.00048	−5	99	165	9	183	3
14JEW12-3-20	354	413	0.86	0.05344	0.00221	0.21180	0.00879	0.02873	0.00034	348	73	195	7	183	2
14JEW12-3-21	381	456	0.83	0.04899	0.00138	0.19433	0.00549	0.02881	0.00032	147	45	180	5	183	2
14JEW12-3-22	733	697	1.05	0.04931	0.00128	0.19657	0.00531	0.02889	0.00034	163	41	182	5	184	2

2015). (2) It is known that amphiboles and clinopyroxenes that formed from basaltic melts are depleted in LREEs and enriched in HREEs, whereas plagioclase is strongly enriched in Eu (Pearce and Norry, 1979; Dostal et al., 1983; Green, 1995; Sun and Liang, 2012). If the monzogranites had formed from a magma generated by fractional crystallization of a primary basic magma, they would have relatively high LREE and low HREE abundances, and significant negative Eu anomalies compared with the mafic rocks. The Tazigou pluton (monzogranite) has lower REE abundances than the other plutons and only moderately negative Eu anomalies. Furthermore, the REE trends of the monzogranites are subparallel to those of the mafic–intermediate intrusions (Fig. 6), indicating that the monzogranites and coeval gabbro–dioritic rocks are not linked by fractional crystallization. It seems more likely that they were derived from separate and independent primary magmas. In contrast, compared with the coeval gabbro–-diorites, the diorites and granodiorites have relatively high LREE and low HREE abundances, consistent with fractional crystallization. In fact, when mantle-derived basaltic magmas underplate and/or intrude the lower crust, they transfer heat into the overlying and surrounding crust, which can lead to partial melting of the wall rocks (Hildreth, 1981; Raia and Spera, 1997; Annen and Sparks, 2002) and the generation of felsic magmas.

Taking all of the above into account, we conclude that the gabbro–diorites, diorites, and granodiorites are related to each other via fractional crystallization from a parental magma, whereas the coeval monzogranites were generated by partial melting of the lower crust.

5.2.2. Magma source of the Early Jurassic mafic intrusive rocks

As discussed above, fractional crystallization played an important role in the formation of the gabbro–diorites (e.g., the Shangnan and Yinxing plutons), diorites (Shangtan Pluton), and granodiorites (Donggou Pluton). To minimize the effects of fractional crystallization, crustal assimilation, and/or magmatic mixing, we focused on the mafic intrusions (Yinxing plutons) since they are likely to provide more direct insights into the nature of the magmatic source.

Given their positive Eu anomalies (Fig. 6a), the mafic rocks discussed here may have experienced crystal accumulation during the early stages of magma evolution. Furthermore, these rocks (Yinxing Pluton) are not primary mantle melts, as indicated by their relatively low values of Mg# (47–48) and low Cr (19.2–20.4 ppm) and Ni (11.0–11.7 ppm) contents (Table 2; Frey and Prinz, 1978; Cox, 1980; Xu et al., 2004).

In consideration of crystal accumulation in mafic intrusions, the whole-rock geochemistry does not reflect the composition of the parental magma; instead, it may reflect the sum of the composition of the accumulative crystals and the trapped melts (Bédard, 1994; Guo et al., 2015). Remarkably, these rocks do share a number of common geochemical features, such as uniformly low SiO_2 concentrations, LREE and LILE enrichments, and HREE and HFSE depletions (Fig. 6), demonstrating the geochemical similarity between these rocks and arc-related igneous rocks elsewhere (Gill, 1981; Grove and Donnelly-Nolan, 1986; Grove et al., 2003; Wilson, 1989; Hawkesworth et al., 1997; Eiler et al., 2000; Elburg et al., 2002; Deering et al., 2007; Meng et al., 2008; Wang et al., 2012). Fortunately, the Lu–Hf isotopic system can be used to track information on the parental magma by virtue of the fact that fractionation of Lu from Hf occurs during magma generation (Kinny et al., 1991; Wu et al., 2007a, 2007b; Yang et al., 2007). The mafic rocks of the present study have $\varepsilon_{Hf}(t)$ values of +8.5 to +9.5 and Hf single-stage (T_{DM1}) model ages of 464–505 Ma, indicating that their magma source isotopically resembles a depleted mantle. Furthermore, the low Nb/La ratios (0.3–0.4) suggest a lithospheric mantle source consistent with the depletion of HFSEs (e.g., Nb and Ta) relative to LREEs in the lithospheric mantle (Smith et al., 1999).

Table 2
Major elements (wt.%) and trace elements (ppm) data for the Early Jurassic igneous rocks in eastern Jilin Province, NE China.

Sample	14JEW2-2	14JEW2-4	14JEW2-5	14JEW3-4	14JEW3-5	14JEW3-6	14JEW8-4	14JEW8-8	14JEW8-9
SiO_2	65.9	65.6	66.2	76.1	75.7	75.8	65.1	61.4	61.4
TiO_2	0.56	0.57	0.56	0.12	0.12	0.12	0.55	0.66	0.63
Al_2O_3	16.1	16.2	15.9	12.8	13.2	13.1	16.6	16.9	17.3
TFe_2O_3	3.90	3.96	3.84	0.99	0.95	0.95	4.63	5.61	5.51
MnO	0.06	0.06	0.07	0.03	0.03	0.03	0.08	0.09	0.09
MgO	1.71	1.74	1.69	0.24	0.23	0.23	1.97	2.55	2.45
CaO	2.99	3.16	3.09	0.85	0.79	0.90	4.13	5.36	5.40
Na_2O	3.88	3.96	3.89	3.62	3.70	3.72	3.81	3.51	3.57
K_2O	3.27	3.14	3.12	3.96	3.83	3.94	1.82	2.21	2.14
P_2O_5	0.14	0.15	0.14	0.04	0.04	0.04	0.11	0.13	0.13
LOI	1.12	1.04	1.12	0.68	0.74	0.58	0.80	0.96	1.10
TOTAL	98.4	98.5	98.5	98.7	98.6	98.8	98.8	98.4	98.6
Mg#	46.5	46.5	46.6	32.4	32.4	32.4	45.7	47.4	46.8
Na_2O/K_2O	1.19	1.26	1.25	0.91	0.97	0.94	2.09	1.59	1.67
A/CNK	1.05	1.03	1.03	1.08	1.13	1.09	1.06	0.95	0.96
Be	1.72	1.69	1.84	1.17	1.23	1.10	1.14	1.06	1.05
Sc	6.77	6.47	6.48	2.34	2.07	2.06	9.06	12.0	12.2
V	61.7	61.6	60.8	8.13	7.53	7.53	82.9	109	110
Cr	14.8	15.3	13.4	1.11	1.16	1.00	19.0	19.0	17.8
Co	8.24	8.20	8.24	0.99	0.95	0.91	10.5	13.5	13.1
Ni	6.13	5.88	5.98	1.08	1.04	0.96	8.57	10.5	9.86
Cu	3.18	3.10	3.26	0.63	0.66	0.51	2.34	16.4	12.6
Zn	46.9	44.7	43.6	15.6	14.8	18.5	57.0	63.3	62.3
Ga	18.7	18.6	19.0	14.4	13.7	13.9	17.5	17.8	18.1
Rb	109	102	99.4	110	99.8	101	70.8	68.2	62.0
Sr	431	429	443	105	98.9	99.1	279	296	310
Y	14.5	14.0	14.2	11.8	8.86	9.25	15.1	16.6	17.7
Zr	193	153	197	61.8	58.9	71.2	109	115	111
Nb	6.55	6.35	6.61	6.26	5.66	5.71	4.32	4.02	3.91
Cs	5.46	5.64	6.24	5.34	4.30	4.49	6.54	5.98	5.20
Ba	544	512	522	689	593	621	396	338	344
La	23.4	25.3	22.7	14.6	13.4	13.6	12.7	11.3	19.2
Ce	46.1	48.9	45.8	30.7	29.1	28.4	30.4	26.0	38.6
Pr	5.19	5.45	5.08	3.30	3.08	3.14	3.44	3.21	4.23
Nd	19.4	19.6	18.5	10.9	10.3	10.5	13.5	13.0	15.6
Sm	3.70	3.67	3.71	2.22	1.93	2.13	2.90	3.01	3.29
Eu	0.95	0.94	0.94	0.42	0.40	0.41	0.83	0.87	0.91
Gd	3.06	3.02	2.99	1.81	1.55	1.61	2.80	2.95	3.21
Tb	0.46	0.45	0.44	0.31	0.27	0.25	0.43	0.49	0.50
Dy	2.61	2.60	2.61	1.83	1.48	1.52	2.63	2.98	3.20
Ho	0.48	0.48	0.50	0.38	0.28	0.29	0.52	0.60	0.61
Er	1.35	1.33	1.35	1.09	0.80	0.83	1.49	1.69	1.74
Tm	0.21	0.19	0.20	0.17	0.13	0.13	0.23	0.25	0.26
Yb	1.41	1.34	1.40	1.14	0.90	0.93	1.60	1.75	1.77
Lu	0.21	0.21	0.22	0.18	0.14	0.14	0.25	0.26	0.27
Hf	5.09	4.16	5.28	2.31	2.15	2.45	3.41	3.32	3.15
Ta	0.55	0.58	0.62	0.59	0.61	0.57	0.53	0.35	0.34
Pb	11.1	10.8	10.3	20.7	19.0	19.2	11.4	12.3	12.1
Th	12.9	12.8	12.5	10.1	9.44	9.05	8.25	4.55	8.73
U	2.47	1.91	2.19	2.54	1.55	1.67	1.79	1.49	2.32
δEu	0.84	0.84	0.84	0.62	0.69	0.65	0.88	0.88	0.85
LREE	98.7	104	96.7	62.1	58.2	58.2	63.8	57.4	81.8
HREE	9.79	9.62	9.71	6.91	5.55	5.70	10.0	11.0	11.6
LREE/HREE	10.1	10.8	10.0	9.0	10.5	10.2	6.41	5.23	7.08
ΣREE	109	113	106	69.1	63.8	63.9	73.7	68.4	93.4
$(La/Yb)_N$	11.9	13.6	11.6	9.19	10.7	10.5	5.70	4.63	7.78

(continued on next page)

Table 2 *(continued)*

Sample	14JEW2-2	14JEW2-4	14JEW2-5	14JEW3-4	14JEW3-5	14JEW3-6	14JEW8-4	14JEW8-8	14JEW8-9
	14JEW8-10	14JEW11-1	14JEW11-3	14JEW11-4	14JEW11-5	14JEW12-3	14JEW12-4	14JEW12-5	14JEW12-6
SiO_2	62.5	52.8	52.8	52.9	51.1	54.9	54.7	54.7	55.0
TiO_2	0.62	1.13	1.14	1.10	1.20	1.04	1.02	1.06	1.05
Al_2O_3	16.9	19.0	19.1	19.2	19.6	20.0	20.2	20.2	20.1
TFe_2O_3	5.34	8.17	8.24	7.93	8.39	6.55	6.38	6.55	6.46
MnO	0.08	0.14	0.13	0.13	0.13	0.10	0.09	0.10	0.09
MgO	2.37	3.70	3.78	3.65	3.93	2.57	2.42	2.59	2.45
CaO	5.13	7.90	8.03	7.69	8.13	7.62	7.72	7.79	7.93
Na_2O	3.53	3.72	3.73	3.88	3.95	4.00	4.09	4.08	4.07
K_2O	2.32	1.31	1.28	1.49	1.20	2.04	1.68	1.76	1.75
P_2O_5	0.12	0.22	0.24	0.22	0.25	0.24	0.28	0.28	0.27
LOI	0.92	1.40	1.38	1.44	1.52	0.82	0.86	0.50	0.80
TOTAL	98.9	98.1	98.5	98.2	97.9	99.1	98.5	99.1	99.1
Mg#	46.8	47.3	47.6	47.7	48.1	43.7	42.9	43.9	42.9
Na_2O/K_2O	1.52	2.84	2.91	2.60	3.29	1.96	2.43	2.32	2.33
A/CNK	0.96	0.87	0.86	0.88	0.87	0.88	0.89	0.89	0.87
Be	1.06	1.03	1.08	0.99	0.98	1.35	1.35	1.23	1.39
Sc	12.0	18.5	19.9	19.0	19.7	11.2	10.3	12.6	12.1
V	107	176	187	178	191	132	126	130	126
Cr	19.2	19.2	20.4	20.1	19.3	12.1	12.1	15.1	12.6
Co	12.8	20.2	20.9	20.7	20.2	14.9	14.3	15.4	14.2
Ni	9.98	11.1	11.4	11.7	11.0	10.7	9.76	12.2	9.67
Cu	12.8	12.2	10.6	11.3	27.2	64.6	34.9	37.9	19.5
Zn	61.1	77.7	78.5	76.3	80.7	75.0	68.5	70.3	69.5
Ga	18.1	19.7	20.7	20.4	20.7	22.4	21.5	22.5	22.9
Rb	68.1	37.3	38.6	44.8	31.6	43.5	43.7	41.4	46.4
Sr	296	645	671	670	717	732	719	749	744
Y	16.9	22.0	22.7	22.4	22.3	20.8	20.0	18.7	19.7
Zr	86.1	75.0	85.5	99.2	104	220	137	104	107
Nb	4.01	4.60	4.70	4.36	4.54	7.62	6.53	6.71	6.54
Cs	5.15	1.48	1.43	1.65	2.25	1.58	2.19	1.61	2.26
Ba	350	445	430	456	489	514	443	504	489
La	12.3	12.6	13.4	12.7	13.3	21.1	20.1	20.0	21.5
Ce	28.3	30.5	32.1	30.8	31.9	43.6	43.5	43.1	46.0
Pr	3.39	4.08	4.32	4.16	4.29	5.40	5.39	5.25	5.59
Nd	13.5	17.9	18.7	18.2	18.3	21.9	21.7	21.8	22.8
Sm	2.98	4.09	4.31	4.12	4.31	4.93	4.63	4.70	4.79
Eu	0.92	1.36	1.43	1.42	1.49	1.66	1.70	1.76	1.73
Gd	2.96	4.10	4.31	4.07	4.32	4.44	4.30	4.43	4.51
Tb	0.49	0.63	0.67	0.65	0.68	0.67	0.66	0.63	0.67
Dy	3.05	3.75	3.90	3.82	3.89	3.81	3.66	3.68	3.77
Ho	0.59	0.75	0.77	0.74	0.78	0.73	0.70	0.69	0.73
Er	1.74	2.09	2.12	2.07	2.14	1.95	1.97	1.82	1.96
Tm	0.25	0.30	0.30	0.30	0.32	0.29	0.27	0.26	0.28
Yb	1.69	1.94	2.04	1.99	2.04	1.86	1.65	1.63	1.78
Lu	0.27	0.29	0.30	0.28	0.31	0.26	0.25	0.24	0.25
Hf	2.51	2.22	2.48	2.75	2.76	5.73	3.58	2.80	3.04
Ta	0.36	0.29	0.32	0.29	0.30	0.51	0.44	0.43	0.44
Pb	13.2	7.32	10.1	7.43	8.22	12.9	12.6	12.0	13.2
Th	4.40	3.22	3.44	3.62	2.14	4.31	4.65	3.57	5.04
U	1.59	0.66	0.93	0.68	1.01	0.98	1.16	0.95	1.35
δEu	0.94	1.01	1.01	1.05	1.05	1.07	1.15	1.16	1.12
LREE	61.4	70.5	74.3	71.4	73.6	98.6	97.0	96.6	102
HREE	11.0	13.9	14.4	13.9	14.5	14.0	13.5	13.4	14.0
LREE/HREE	5.56	5.09	5.15	5.13	5.08	7.04	7.21	7.22	7.34
ΣREE	72.4	84.4	88.7	85.3	88.1	113	110	110	116
$(La/Yb)_N$	5.22	4.66	4.71	4.58	4.68	8.14	8.74	8.81	8.67

Note: LOI: Loss on ignition; Mg# = $Mg^{2+}/(Mg^{2+} + TFe^{2+})$; A/CNK = mole $[Al_2O_3/(CaO + Na_2O + K_2O)]$; δEu = (Eu)cn/[(Gd)cn + (Sm)cn]/2; $(La/Yb)_N$ = (La/0.687)/(Yb/0.493).

Table 3
Lu–Hf isotopic data for the Early Jurassic igneous rocks in eastern Jilin Province, NE China.

Sample no.	t (Ma)	$^{176}Yb/^{177}Hf$	1σ	$^{176}Lu/^{177}Hf$	1σ	$^{176}Hf/^{177}Hf$	1σ	$e_{Hf}(0)$	1σ	$e_{Hf}(t)$	1σ	T_{DM1}(Hf) (Ma)	T_{DM2}(Hf) (Ma)	$f_{Lu/Hf}$
14JEW2-1 Donggou pluton (granodiorite)														
14JEW2-1-01	183	0.015628	0.000205	0.000659	0.000009	0.282901	0.000010	4.6	0.6	8.5	0.6	493	619	−0.98
14JEW2-1-02	183	0.020851	0.000128	0.000905	0.000005	0.282909	0.000010	4.8	0.6	8.8	0.6	485	605	−0.97
14JEW2-1-03	183	0.022051	0.000307	0.000934	0.000013	0.282882	0.000010	3.9	0.6	7.8	0.6	523	658	−0.97
14JEW2-1-04	183	0.020160	0.000369	0.000867	0.000014	0.282881	0.000010	3.9	0.6	7.8	0.6	523	660	−0.97
14JEW2-1-05	183	0.020595	0.000208	0.000893	0.000012	0.282887	0.000009	4.1	0.6	8.0	0.6	516	648	−0.97
14JEW2-1-06	183	0.015593	0.000124	0.000685	0.000005	0.282888	0.000011	4.1	0.6	8.1	0.6	511	645	−0.98
14JEW2-1-07	183	0.036988	0.000872	0.001510	0.000032	0.282882	0.000012	3.9	0.7	7.7	0.7	532	663	−0.95
14JEW2-1-08	183	0.023664	0.000188	0.001004	0.000007	0.282897	0.000012	4.4	0.7	8.3	0.7	503	629	−0.97
14JEW3-1 Tazigou pluton (monzogranite)														
14JEW3-1-01	183	0.027045	0.000689	0.001169	0.000031	0.282883	0.000012	3.9	0.7	7.8	0.7	526	659	−0.96
14JEW3-1-02	183	0.038841	0.001018	0.001580	0.000043	0.282855	0.000012	2.9	0.7	6.7	0.7	572	718	−0.95
14JEW3-1-03	183	0.045884	0.001088	0.001820	0.000040	0.282879	0.000010	3.8	0.6	7.6	0.6	541	671	−0.95
14JEW3-1-04	183	0.018442	0.001273	0.000789	0.000057	0.282893	0.000010	4.3	0.6	8.2	0.6	506	636	−0.98
14JEW3-1-05	183	0.020802	0.000477	0.000978	0.000023	0.282891	0.000012	4.2	0.7	8.1	0.7	511	641	−0.97
14JEW3-1-06	183	0.061352	0.002040	0.002472	0.000081	0.282911	0.000014	4.9	0.7	8.7	0.7	502	611	−0.93
14JEW3-1-07	183	0.070256	0.001183	0.002810	0.000035	0.282899	0.000013	4.5	0.7	8.2	0.7	526	638	−0.92
14JEW3-1-08	183	0.053462	0.001555	0.002162	0.000063	0.282917	0.000014	5.1	0.7	8.9	0.7	489	597	−0.93
14JEW8-1 Shangtan (diorite)														
14JEW8-1-01	183	0.020733	0.000631	0.000849	0.000025	0.282923	0.000010	5.3	0.6	9.3	0.6	464	577	−0.97
14JEW8-1-02	183	0.016865	0.000260	0.000716	0.000011	0.282935	0.000010	5.8	0.6	9.7	0.6	446	553	−0.98
14JEW8-1-03	183	0.029777	0.000151	0.001264	0.000006	0.282929	0.000011	5.6	0.7	9.4	0.7	461	567	−0.96
14JEW8-1-04	183	0.016225	0.000108	0.000668	0.000003	0.282911	0.000010	4.9	0.6	8.9	0.6	479	599	−0.98
14JEW8-1-05	183	0.018024	0.000244	0.000741	0.000009	0.282920	0.000014	5.2	0.7	9.2	0.7	468	583	−0.98
14JEW8-1-06	183	0.014365	0.000256	0.000673	0.000010	0.282922	0.000012	5.3	0.7	9.2	0.7	464	578	−0.98
14JEW8-1-07	183	0.013284	0.000275	0.000600	0.000013	0.282900	0.000012	4.5	0.7	8.5	0.7	494	621	−0.98
14JEW8-1-08	183	0.018600	0.000105	0.000782	0.000004	0.282946	0.000012	6.2	0.7	10.1	0.7	430	530	−0.98
14JEW11-1 Yinxing pluton (gabbro-diorite)														
14JEW11-1-01	185	0.042920	0.000955	0.001928	0.000044	0.282923	0.000014	5.3	0.7	9.2	0.7	478	584	−0.94
14JEW11-1-02	185	0.039857	0.004708	0.001784	0.000203	0.282931	0.000014	5.6	0.7	9.5	0.7	465	567	−0.95
14JEW11-1-03	185	0.050463	0.001510	0.002245	0.000066	0.282931	0.000013	5.6	0.7	9.4	0.7	471	571	−0.93
14JEW11-1-04	185	0.049722	0.001973	0.002173	0.000086	0.282909	0.000012	4.9	0.7	8.7	0.7	502	613	−0.93
14JEW11-1-05	185	0.019627	0.001123	0.000878	0.000046	0.282924	0.000014	5.4	0.7	9.3	0.7	464	575	−0.97
14JEW11-1-06	185	0.046475	0.001462	0.002144	0.000060	0.282927	0.000013	5.5	0.7	9.3	0.7	476	578	−0.94
14JEW11-1-07	185	0.044069	0.001397	0.001983	0.000057	0.282905	0.000015	4.7	0.7	8.5	0.7	505	620	−0.94
14JEW11-1-08	185	0.058654	0.003022	0.002532	0.000128	0.282924	0.000015	5.4	0.7	9.1	0.7	484	585	−0.92
14JEW12-3 Shangnan pluton (gabbro-diorite)														
14JEW12-3-01	183	0.014238	0.000267	0.000551	0.000010	0.282734	0.000014	−1.3	0.7	2.6	0.7	725	948	−0.98
14JEW12-3-02	183	0.065311	0.001382	0.002336	0.000051	0.282725	0.000011	−1.7	0.6	2.1	0.7	774	978	−0.93
14JEW12-3-03	183	0.065429	0.000762	0.002428	0.000025	0.282763	0.000014	−0.3	0.7	3.4	0.7	720	904	−0.93
14JEW12-3-04	183	0.050311	0.000522	0.001834	0.000019	0.282735	0.000010	−1.3	0.6	2.5	0.6	749	956	−0.94
14JEW12-3-05	183	0.019503	0.000755	0.000729	0.000026	0.282748	0.000014	−0.8	0.7	3.1	0.7	709	922	−0.98
14JEW12-3-06	183	0.047747	0.002745	0.001764	0.000102	0.282735	0.000013	−1.3	0.7	2.5	0.7	748	955	−0.95
14JEW12-3-07	183	0.018181	0.000345	0.000692	0.000013	0.282739	0.000010	−1.2	0.6	2.8	0.6	721	939	−0.98
14JEW12-3-08	183	0.031915	0.001006	0.001167	0.000035	0.282737	0.000012	−1.2	0.7	2.6	0.7	733	947	−0.96

Experimental studies (e.g., Tatsumi et al., 1986) have shown enhanced mobility of LILEs in hydrous fluids compared with REEs and HFSEs, and thus the LILE enrichment associated with HFSE depletion is commonly attributed to the presence of a fluid component (Gill, 1981; Arculus and Powell, 1986). The high Th/Zr and Rb/Y, and low Nb/Zr and Nb/Y ratios (Fig. 10) of the mafic intrusive rocks in this study also indicate that their mantle source had been metasomatized by subduction-related fluids rather than by hydrous melts (Kepezhinskas et al., 1997). Fluids derived from different subducted components have distinct geochemical features. Specifically, fluids derived from altered oceanic crust (AOC) are distinguishable from fluids derived from dewatered sediments on a plot of Ba/Zr versus Th/Zr (Ishuzuka et al., 2003; Fig. 11). The mafic intrusions in this study have high Ba/Zr and Th/Zr ratios, and plot between AOC-released fluids and the bulk sediment mixing line in Fig. 11. It therefore seems likely that fluids both from sediments and AOC were added to the mantle wedge from which the calc-alkaline magmas were produced. Additionally, it has been widely suggested that Th, Ba, and the REEs exhibit different geochemical behaviors in slab-derived fluids and melts (Ayers, 1998; Kogiso et al., 1997; Guo et al., 2009, 2015; Spandler and Pirard, 2013). This phenomenon can be used to effectively distinguish the possible roles of the fluids and melts derived from the subducted oceanic crust and its overlying sediments. As a consequence, the higher Th/Sm (0.5–1.05), Th/Ce (0.07–0.11), Ba/La (22.1–36.8), and Th/Yb (1.05–2.82) ratios suggest that the mafic intrusions in this study show a predominant sediment-melt contribution to the mantle source (Guo et al., 2015).

5.2.3. Magma source of the Early Jurassic monzogranites

Samples of the Tazigou monzogranite are characterized by high SiO_2 and K_2O, and low MgO, TFe_2O_3, and CaO as well as low Cr and Ni values, which is not in equilibrium with the mantle assemblage (Kaygusuz and Öztürk, 2015). As mentioned above, the monzogranites and coeval gabbro–dioritic rocks are not linked by fractional crystallization, and the REE trends are subparallel to those of the mafic–intermediate intrusions (Fig. 6). These samples show negative Nb, Ta, and Ti, and positive Th and K anomalies. In addition, they show LILE and LREE enrichment (Fig. 6), which is common in crustal rocks (Kaygusuz and Öztürk, 2015). Furthermore, the Nb/Ta and Zr/Sm ratios of the Tazigou monzogranites range from 9 to 11 and 29 to 33, respectively (Table 2), similar to the average ratios of crust-derived magmas (Green, 1995; Kaygusuz and Öztürk, 2015). On the other hand, the Tazigou monzogranites have relatively low total REE abundances, relatively high HREE abundances, and moderately negative Eu anomalies (Fig. 6), indicating that plagioclase rather than garnet was a residue in the magma source. The $\varepsilon_{Hf}(t)$ values and T_{DM2} of the zircons range from +6.7 to +8.9 and from 597 to 718 Ma, respectively, indicating that the magma source was a depleted crust accreted during the Neoproterozoic. Considering the above, we conclude that the primary magma for the Early Jurassic monzogranites was derived from partial melting of a depleted lower-crustal block that was accreted during the Neoproterozoic.

5.3. Implications for subduction of the Paleo-Pacific Plate beneath Eurasia

The initiation of Paleo-Pacific Plate subduction beneath Eurasia has been variously assigned to the early Permian (Ernst et al., 2007; Sun et al., 2015), the Triassic (Zhao et al., 1996; Zhou et al., 2014; Wilde, 2015; Yang et al., 2015), and the Early–Middle Jurassic (Zhao et al., 1994; Sun et al., 2005; Wu et al., 2007a; Pei et al., 2008; Zhou et al., 2009; Yu et al., 2012; Xu et al., 2013a, 2013b; Wang et al., 2015; Guo et al., 2015; Guo, 2016). In the eastern part of NE China, Permian–Jurassic igneous rock associations and their spatial distribution, together with their tectonic evolution history, are key to discussions of the subduction history of the Paleo-Pacific Plate beneath the Eurasian continent.

Permian magmatism in the eastern part of NE China is found mainly along the northern margin of the NCC and the eastern margin of the Jiamusi Massif (Cao et al., 2013; Meng et al., 2008; Fig. 12). In the former case, the igneous rocks are mainly calc-alkaline and record the southward subduction of the Paleo-Asian Oceanic Plate beneath the NCC (Cao et al., 2012, 2013); in the latter case, the igneous rocks form a calc-alkaline suite that most likely records the subduction of the Paleo-Asian Oceanic Plate or an unnamed plate beneath the Jiamusi Massif (Meng et al., 2008; Isozaki et al., 2010; Bi et al., 2015; Yang et al., 2015).

The Paleo-Asian Ocean between North China and Siberia was narrowed by a complex subduction system that was active in the Triassic (Isozaki et al., 2010; Cao et al., 2013; Wang et al., 2016). Along the Pacific margin of South China, the active subduction of the Farallon Plate formed the Triassic ACs and meta-ACs (the Suo and Ultra-Tanba belts), whereas the tectonic evolution of NE China was related to the closure of the Paleo-Asian Ocean during the Late Triassic. A series of late Paleozoic and early Mesozoic igneous rocks and metamorphism along the northern margin of the NCC represent the response to the final closure of the Paleo-Asian Ocean during the latest Permian and Early Triassic along the Solonker–Xar Moron–Changchun–Yanji zone (Sun et al., 2004; Li et al., 2007; Wu et al., 2007a; Cao et al., 2013; Xu et al., 2013a, 2013b). This view is supported by the passive continental margin sedimentation of the Late Triassic Nanshuangyashan Formation along the eastern margin of the Jiamusi Massif (Zhang et al., 2014). It is thus unreasonable to attribute the initial subduction of the Paleo-Pacific Plate to the Triassic.

The compilation of the presently available data illustrated in Fig. 12 outlines the distribution of Early Jurassic igneous rocks (both volcanic and intrusive) in NE China (Kim et al., 2003, 2005; Oh et al., 2004; Han et al., 2006; Wu et al., 2007a, 2011; Park et al., 2009; Kee et al., 2010; Xu et al., 2013a, 2013b). Notably, these rocks are distributed within a NE-trending belt sub-parallel to the eastern margin of Eurasia and perpendicular to the direction of Paleo-Pacific Plate movement at that time (Engebretson et al., 1985). The Early Jurassic magmatic rocks in the eastern part of Jilin Province are mainly calc-alkaline intrusive rocks such as gabbro, diorite, granodiorite, and monzogranite, typical indicators of an active continental margin setting (Miyashiro, 1974; Ewart, 1982; Tang et al., 2015; Fig. 13). Thus, the Early Jurassic igneous rocks of NE China represent the response to the subduction of the Paleo-Pacific Plate beneath Eurasia. This interpretation is further supported by the occurrence of contemporaneous bimodal igneous rocks in the Lesser Xing'an–Zhangguangcai Ranges (Yu et al., 2012; Xu et al., 2013a, 2013b; Fig. 13). The variation in the Early Jurassic igneous rocks, from continental margin calc-alkaline associations to intra-continental bimodal associations, is best explained by westward subduction of the Paleo-Pacific Plate beneath the Eurasian continent in the Early Jurassic (Xu et al., 2013a). In this model, the calc-alkaline associations represent continental arc magmatism and the bi-modal associations, located farther west, represent magmatism in a back-arc setting. Early Jurassic accretionary complexes that are related to the subduction of the Paleo-Pacific Plate have been widely identified along the eastern margin of Eurasia (Safonova and Santosh, 2014), including in Japan (Fukuyama et al., 2013).

6. Conclusions

1. A suite of Early Jurassic (183–185 Ma) calc-alkaline intrusive rocks, including gabbro–diorite, diorite, granodiorite, and monzogranite, is identified in eastern Jilin Province, NE China.
2. The Early Jurassic mafic and dioritic rocks formed via fractional crystallization of a basaltic parental magma that was derived from partial melting of a lithospheric mantle modified by subduction-related fluids. In contrast, the parental magma of the Early Jurassic monzogranites was probably derived directly from the partial melting of a Neoproterozoic lower crust.
3. The Early Jurassic calc-alkaline igneous rocks in NE China form a NE-trending belt along an active continental margin, perpendicular to the contemporary movement direction of the Paleo-Pacific Plate. Thus, they probably represent the magmatic response to initial subduction of the Paleo-Pacific Plate beneath Eurasia in the Mesozoic.

Acknowledgments

This work was financially supported by the National Natural Science Foundation of China (Grants 41330206 and 41402043), the Strategic Priority Research Program of the Chinese Academy of Sciences (Grant

No. XDB18030604) and the China Postdoctoral Science Foundation (Grant 2014M560679).

References

Anderson, T., 2002. Correction of common lead in U-Pb analyses that do not report ^{204}Pb. Chem. Geol. 192, 59–79.
Annen, C., Sparks, R.S.J., 2002. Effects of repetitive emplacement of basaltic intrusions on thermal evolution and melt generation in the crust. Earth Planet. Sci. Lett. 203, 937–955.
Arculus, R.J., Powell, R., 1986. Source component mixing in the region of arc magma generation. J. Geophys. Res. 91, 5913–5926.
Ayers, J., 1998. Trace element modeling of aqueous fluid–peridotite interaction in the mantle wedge of subduction zones. Contrib. Miner. Petrol. 132, 390–404.
Bédard, J.H., 1994. A procedure for calculating the equilibrium distribution of trace elements among the minerals of cumulate rocks, and the concentration of trace elements in the coexisting liquids. Chem. Geol. 118, 143–153.
Bi, J.H., Ge, W.C., Yang, H., Zhao, G.C., Xu, W.L., Wang, Z.H., 2015. Geochronology, geochemistry and zircon Hf isotopes of the Dongfanghong gabbroic complex at the eastern margin of the Jiamusi Massif, NE China: petrogensis and tectonic implications. Lithos 234–235, 27–46.
Boynton, W.V., 1984. Geochemistry of the rare earth elements: meteorite studies. In: Henderson, P. (Ed.), Rare Earth Element Geochemistry. Elsevier, pp. 63–114.
Cao, H.H., Xu, W.L., Pei, F.P., Guo, P.Y., Wang, F., 2012. Permian tectonic evolution of the eastern section of the northern margin of the North China Plate: constraints from zircon U-Pb geochronology and geochemistry of the volcanic rocks. Acta Petrol. Sin. 28, 2733–2750 (in Chinese with English abstract).
Cao, H.H., Xu, W.L., Pei, F.P., Wang, Z.W., Wang, F., Wang, Z.J., 2013. Zircon U-Pb geochronology and petrogenesis of the Late Paleozoic-Early Mesozoic intrusive rocks in the eastern segment of the northern margin of the North China Block. Lithos 170–171, 191–207.
Chen, Y.J., Zhang, C., Li, N., Yang, Y.F., Deng, K., 2012. Geology of the Mo deposits in Northeast China. J. Jilin Univ. (Earth Sci. Ed.) 42, 1223–1267 (in Chinese with English abstract).
Cox, K.G., 1980. A model for flood basalt volcanism. J. Petrol. 21, 629–650.
Deering, C.D., Vogel, T.A., Patino, L.C., Alvarado, G.E., 2007. Origin of distinct silicic magma types from the Guachipelín Caldera, NW Costa Rica: evidence for magma mixing and protracted subvolcanic residence. J. Volcanol. Geoth. Res. 165, 103–126.
Deng, J., Yuan, W.M., Carranza, E.J.M., Yang, L.Q., Wang, C.M., 2014. Geochronology and thermochronometry of the Jiapigou gold belt, northeastern China: new evidence for multiple episodes of mineralization. J. Asian Earth Sci. 89, 10–27.
Dostal, J., Dupuy, C., Carron, J.P., Le, G.M.M., Maury, R.C., 1983. Partition coefficients of trace elements: application to volcanic rocks of St Vincent, West Indies. Geochim. Cosmochim. Acta 47, 525–533.
Eiler, J.M., Grawford, A.J., Elliott, T.R., Farley, K.A., Valley, J.W., Stolper, E., 2000. Oxygen isotope geochemistry of oceanic arc lavas. J. Petrol. 41, 229–256.
Elburg, M.A., Bergen, M.V., Hoogewerff, J., Foden, J., Vroon, P., Zulkarnain, I., Nasution, A., 2002. Geochemical trends across an arc-continent collision zone: magma sources and slab-wedge transfer processes below the Pantar Strait volcanoes, Indonesia. Geochim. Cosmochim. Acta 66, 2771–2789.
Engebretson, D.C., Cox, A., Gordon, R.G., 1985. Relative motions between oceanic and continental plates in the pacific basin. In: vol. 206. Geological Society of America, Special Publications, pp. 1–59.
Ernst, W.G., Tsujimori, T., Zhang, R., Liou, J.G., 2007. Permo-Triassic collision, subduction-zone metamorphism, and tectonic exhumation along the East Asian continental margin. Annu. Rev. Earth Planet. Sci. 35, 73–110.
Ewart, A., 1982. The mineralogy and petrology of Tertiary-Recent orogenic volcanic rocks: with special reference to the andesitic-basaltic compositional range. In: Thorpe, R.S. (Ed.), Andesites: Orogenic Andesites and Related Rocks. Wiley, New York, pp. 25–95.
Frey, F.A., Prinz, M., 1978. Ultramafic inclusions from San Carlos, Arizona: petrologic and geochemical data bearing on their petrogensis. Earth Planet. Sci. Lett. 38, 129–176.
Fukuyama, M., Ogasawara, M., Horie, K., Lee, D.C., 2013. Genesis of jadeite–quartz rocks in the Yorii area of the Kanto Mountains, Japan. J. Asian Earth Sci. 63, 206–217.
Gill, J.B., 1981. Orogenic Andesites and Plate Tectonics. Springer Verlag, New York, pp. 385.
Green, T.H., Sie, S.H., Ryan, C.G., Cousens, D.R., 1989. Proton microprobe-determined partitioning of Nb, Ta, Zr, Sr and Y between garnet, clinopyroxene and basaltic magma at high pressure and temperature. Chem. Geol. 74, 201–216.
Green, T.H., 1995. Significance of Nb/Ta as an indicator of geochemical processes in the crust–mantle system. Chem. Geol. 120, 347–359.
Grove, T.L., Donnelly-Nolan, M., 1986. The evolution of young silic lavas at Medicine Lake Volcano, California: implications for the origin of compositional gaps in calcalkaline series lavas. Contrib. Miner. Petrol. 92, 281–302.
Grove, T.L., Elkins Tanton, L.T., Parman, S.W., Cartterjee, N., Muntener, O., Gaetani, G.A., 2003. Fractional crystallization and mantle melting controls on calk-alkaline differentiation trends. Contrib. Miner. Petrol. 145, 515–533.
Guo, F., Fan, W.M., Li, C.W., Miao, L.C., Zhao, L., 2009. Early Paleozoic subduction of the Paleo-Asian Ocean: evidence from the geochronology and geochemistry of Dashizhai basalts from the Nei Mongolia region, NE China. Sci. Chin. Ser. D – Earth Sci. 52, 940–951.
Guo, F., Li, H.X., Fan, W.M., Li, J.Y., Zhao, L., Huang, M.W., Xu, W.L., 2015. Early Jurassic subduction of the Paleo-Pacific Ocean in NE China: petrologic and geochemical evidence from the Tumen mafic intrusive complex. Lithos 224–225, 46–60.
Guo, F., 2016. Geological records of the Pacific Plate subduction in the northeast Asian continental magin: an overview. Bull. Mineral. Petrol. Geochem. 35 (6), 1082–1092.
Han, R.H., Ree, J.H., Cho, D.L., Kwon, S.T., Armstrong, R., 2006. SHRIMP U-Pb zircon ages of pyroclastic rocks in the Bansong Group, Taebaeksan Basin, South Korea and their implication for the Mesozoic tectonics. Gondwana Res. 9, 106–117.
Hawkesworth, C.J., Turner, S.P., McDermott, F., Peate, D.W., Van Calsteren, P., 1997. U-Th isotopes in arc magmas: implications for element transfer from the subducted crust. Sciences 276, 551–555.
HBGMR (Heilongjiang Bureau of Geology and Mineral Resources), 1993. Regional Geology of Heilongjiang Province. Geological publishing House, Beijing, pp. 1–734 (in Chinese with English abstract).
He, X.D., Zhang, C., Geng, R., Lei, C.C., Guan, Q.B., Liu, J.X., 2014. Geochronology, petrogeochemistry and geologic implication of the Yueshandong diorite pluton in Yanbian Area, Jilin Province. Geol. Resour. 23, 42–50 (in Chinese with English abstract).
He, Z.J., Li, J.Y., Niu, B.G., Ren, J.S., 1998. A late Jurassic intense thrusting-uplifting event in the Yanshan-Yinshan area, Northern China, and its sedimentary response. Geol. Rev. 44, 407–418 (in Chinese with English abstract).
Hildreth, W., 1981. Gradients in silicic magma chambers: implications for lithospheric magmatism. J. Geophys. Res. 86, 10153–10192.
Hu, Z.C., Gao, S., Liu, Y.S., Hu, S.H., Chen, H.H., Yuan, H.L., 2008. Signal enhancement in laser ablation ICP-MS by addition of nitrogen in the central channel gas. J. Anal. At. Spectrom. 23, 1093–1101.
Hu, Z.C., Liu, Y.S., Gao, S., Liu, W.G., Yang, L., Zhang, W., Tong, X.R., Lin, L., Zong, K.Q., Li, M., Chen, H.H., Zhou, L., 2012a. Improved in situ Hf isotope ratio analysis of zircon using newly designed X skimmer cone and Jet sample cone in combination with the addition of nitrogen by laser ablation multiple collector ICP-MS. J. Anal. At. Spectrom. 27, 1391–1399.
Hu, Z.C., Liu, Y.S., Gao, S., Xiao, S.Q., Zhao, L.S., Günther, D., Li, M., Zhang, W., Zong, K.Q., 2012b. A "wire" signal smoothing device for laser ablation inductively coupled plasma mass spectrometry analysis. Spectrochim. Acta B 78, 50–57.
Irvine, T.H., Baragar, W.R.A., 1971. A guide to the chemical classification of the common volcanic rocks. Can. J. Earth Sci. 8, 523–548.
Ishuzuka, O., Taylor, R.N., Milton, A., Nesbitt, R.W., 2003. Fluid–mantle interaction in an intra-oceanic arc: constraints from high precision Pb isotopes. Earth Planet. Sci. Lett. 211, 221–236.
Isozaki, Y., Aoki, K., Nakama, T., Yanai, S., 2010. New insight into a subduction-related orogen: a reappraisal of the geotectonic framework and evolution of the Japanese Islands. Gondwana Res. 18, 82–105.
Jahn, B.M., 2004. The Central Asian Orogenic Belt and growth of the continental crust in the Phanerozoic. In: In: Malpas, J., Fletcher, C.J.N., Ali, J.R., Aitchison, J.C. (Eds.), Aspects of the Tectonic Evolution of China, vol. 226. Geological Society London Special Publication, pp. 73–100.
JBGMR (Jilin Bureau of Geology and Mineral Resources), 1988. Regional Geology of Jilin Province. Geological Publishing Housepp. 1–698 (in Chinese with English summary).
JBGMR (Jilin Bureau of Geology and Mineral Resources), 2007. Report of 1:250,000 Regional Geological Research (Wangqing-chunhua and Yanji-Madida Sheets).
Kaygusuz, A., Öztürk, M., 2015. Geochronology, geochemistry, and petrogenesis of the Eocene Bayburt intrusions, Eastern Pontides, NE Turkey: evidence for lithospheric mantle and lower crustal sources in the high-K calc-alkaline magmatism. J. Asian Earth Sci. 108, 97–116.
Kee, W.S., Kim, S.W., Jeong, Y.J., Kwon, S., 2010. Characteristics of Jurassic continental arc magmatism in South Korea: tectonic implications. J. Geol. 118, 305–323.
Keller, C.B., Schoene, B., Barboni, M., Samperton, K.M., Husson, J.M., 2015. Volcanic–plutonic parity and the differentiation of the continental crust. Nature 523, 301–319.
Kepezhinskas, P., McDermott, F., Defant, M.J., Hochstaedter, A., Drummond, M.S., Hawkesworth, C.J., Koloskov, A., Maury, R.C., Bellon, H., 1997. Trace element and Sr-Nd-Pb isotopic constraints on a three-component model of Kamchatka Arc petrogenesis. Geochim. Cosmochim. Acta 61, 577–600.
Kim, C.B., Chang, H.W., Turek, A., 2003. U-Pb zircon ages and Sr–Nd–Pb isotopic compositions for Permian-Jurassic plutons in the Ogcheon belt and Ryeongnam massif, Korea: tectonic implications and correlation with the China Qinling-Dabie belt and the Japan Hida belt. Island Arc 12, 366–382.
Kim, S.W., Oh, C.W., Choi, S.G., Ryu, I.-C., Itaya, T., 2005. Ridge subduction-related Jurassic plutonism in and around the Okcheon metamorphic belt, South Korea, and implications for northeast Asian tectonics. Int. Geol. Rev. 47, 248–269.
Kinny, P.D., Compston, W., Williams, I.S., 1991. A reconnaissance ion-probe study of hafnium isotopes in zirconcs. Geochim. Cosmochim. Acta 55, 849–859.
Kogiso, T., Tatsumi, Y., Nakano, S., 1997. Trace element transport during dehydration processes in the subducted oceanic crust: 1. Experiments and implications for the origin of oceanic island basalts. Earth Planet. Sci. Lett. 148, 193–205.
Koschek, G., 1993. Origin and significance of the SEM cathodoluminescence from zircon. J. Microsc. 171, 223–232.
Lei, C.C., Li, S.C., Liu, Z.H., Xu, Z.Y., Zhang, C., Bai, X.H., 2014. Petrogenesis and tectonic setting of Mingnandong pluton in Yanbian Area: constraints from petro-geochemistry and zircon U-Pb ages. Geol. Chin. 41, 1328–1340 (in Chinese with English abstract).
Li, C.Y., Zhang, H., Wang, F.Y., Sun, Y.L., Sun, W.D., 2012. The formation of the Dabaoshan porphyry molybdenum deposit: a slab rollback model. Lithos 150, 101–110.
Li, J.Y., 1998. Some new ideas on tectonics of NE China and its neighboring areas. Geol. Rev. 4, 339–347 (in Chinese with English abstract).
Li, J.Y., Niu, B.G., Song, B., Xu, W.X., Zhang, Y.H., Zhao, Z.R., 1999. Crustal Formation and Evolution of Northern Changbai Mountains, Northeast China. Geological

Publishing House, Beijing, pp. 1–137 (in Chinese with English abstract).
Li, J.Y., 2006. Peimian geodynamic setting of Northeast China and adjacent regions: closure of the Paleo-Asian Ocean and subduction of the Paleo-Pacific Plate. J. Asian Earth Sci. 26, 207–224.
Li, J.Y., Gao, L.M., Sun, G.H., Li, Y.P., Wang, Y.B., 2007. Shuangjingzi middle Triassic syn-collisional crust-derived granite in the east Inner Mongolia and its constraint on the timing of collision between Siberian and Sino-Korean paleo-plates. Acta Petrol. Sin. 23, 565–582 (in Chinese with English abstract).
Ludwig, K.R., 2003. ISOPLOT 3: a geochronological toolkit for Microsoft excel. Berkeley Geochronol. Centre Spec. Publ. 4, 74.
Liu, J.L., Sun, F.Y., Lin, B.L., Wang, Y.D., Wang, S., Hu, A.X., 2015. Geochronology, geochemistry and zircon Hf isotope of Miantian granodiorite intrusion in Yanbian Region, southern Jilin Province and its geological significance. Earth Sci.-J. Chin. Univ. Geosci. 40, 49–60 (in Chinese with English abstract).
Liu, Y.S., Hu, Z.C., Gao, S., Günther, D., Xu, J., Gao, C.G., Chen, H.H., 2008. In situ analysis of major and trace elements of anhydrous minerals by LA-ICP-MS without applying an internal standard. Chem. Geol. 257, 34–43.
Liu, Y.S., Gao, S., Hu, Z.C., Gao, C.G., Zong, K.Q., Wang, D.B., 2010. Continental and oceanic crust recycling-induced melt-peridotite interactions in the Trans-North China Orogen: U-Pb dating, Hf isotopes and trace elements in zircons of mantle xenoliths. J. Petrol. 51, 537–571.
Maniar, P.D., Piccoli, P.M., 1989. Tectonic discrimination of granitoids. Geol. Soc. Am. Bull. 101, 635–643.
Meng, E., Xu, W.L., Pei, F.P., Yang, D.B., Ji, W.Q., Yu, Y., Zhang, X.Z., 2008. Chronology of Late Paleozoic volcanism in eastern and southeastern margin of Jiamusi Massif and its tectonic implications. Chin. Sci. Bull. 53, 1231–1245.
Miyashiro, A., 1974. Volcanic rock series in island arcs and active continental margin. Am. J. Sci. 274, 321–335.
Oh, C.W., Kim, S.W., Ryu, I.C., Okada, T., Hyodo, H., Itaya, T., 2004. Tectono-metamorphic evolution of the Okcheon metamorphic belt, South Korea: tectonic implications in East Asia. Island Arc 13, 387–402.
Park, Y.S., Kim, S.W., Kee, W.S., Jeong, Y.J., Yi, K., Kim, J., 2009. Middle Jurassic tectono-magmatic evolution in the southwestern margin of the Gyeonggi Massif, South Korea. Geosci. J. 13, 217–231.
Pearce, J.A., Norry, M.J., 1979. Petrogenetic implications of Ti, Zr, Y and Nb variations in volcanic rocks. Contrib. Miner. Petrol. 69, 33–47.
Peccerillo, A., Taylor, A.R., 1976. Geochemistry of Eocene calc-alkaline volcanic rocks from the Kastamonu area, Northern Turkey. Contrib. Miner. Petrol. 58, 63–81.
Pei, F.P., Xu, W.L., Yang, D.B., Ji, W.Q., Yu, Y., Zhang, X.Z., 2008. Mesozoic volcanic rocks in the southern Songliao basin: zircon U-Pb ages and their constraints on the nature of basin basement. Earth Sci. (J. Chin. Univ. Geosci.) 5, 603–617 (in Chinese with English abstract).
Peng, Y.J., Qi, C.D., Zhou, X.D., Lu, X.B., Dong, H.C., Li, Z., 2012. Transition from Paleo-Asian Ocean domain to circum-Pacific Ocean domain for the Ji-Hei composite Orogenic belt: time mark and relationship to global tectonics. Geol. Resour. 21, 261–265 (in Chinese with English abstract).
Polat, A., Hofmann, A.W., Rosing, M.T., 2002. Boninite-like volcanic rocks in the 3.7–3.8 Ga Isua greenstone belt, West Greenland: geochemical evidence for intra-oceanic subduction zone processes in the early Earth. Chem. Geol. 184 (3), 231–254.
Pupin, J.P., 1980. Zircon and granite petrology. Contrib. Miner. Petrol. 73, 207–220.
Raia, F., Spera, F.J., 1997. Simulations of crustal anatexis; implications for the growth and differentiation of continental crust. J. Geophys. Res. 102, 22629–22648.
Rudnick, R.L., Gao, S., Ling, W.L., Liu, Y.S., McDonough, W.F., 2004. Petrology and geochemistry of spinel peridotite xenoliths from Hannuoba and Qixia, North China Craton. Lithos 77, 609–637.
Safonova, I.Y., Santosh, M., 2014. Accretionary complexes in the Asia-Pacific region: tracing archives of ocean plate stratigraphy and tracking mantle plumes. Gondwana Res. 25, 126–158.
Sengör, A.M.C., Natal'in, B.A., Burtman, V.S., 1993. Evolution of the Altaid tectonic collage and Paleozoic crustal growth in Eurasia. Nature 364, 299–307.
Sengör, A.M.C., Natal'in, B.A., 1996. Paleotectonics of Asia: fragments of a synthesis. In: Yin, A., Harrison, M. (Eds.), The Tectonic Evolution of Asia. Cambridge University Press, Cambridge, pp. 486–640.
Smith, E.I., Sanchez, A., Walker, J.D., Wang, K., 1999. Geochemistry of mafic magmas in the Hurricane Volcanic field, Utah: implications for small- and large-scale chemical variability of the lithospheric mantle. J. Geol. 107, 433–448.
Spandler, C., Pirard, C., 2013. Element recycling from subducting slabs to arc crust: a review. Lithos 170–171, 208–223.
Sun, C.G., Liang, Y., 2012. Distribution of REE between clinopyroxene and basaltic melt along a mantle adiabat: effects of major element composition, water, and temperature. Contrib. Miner. Petrol. 163, 807–823.
Sun, D.Y., Wu, F.Y., Zhang, Y.B., Gao, S., 2004. The final closing time of Xiramuron-Changchun-Yanji plate suture zone: evidence from the Dayushan granitic pluton of Jilin. J. Jilin Univ. (Earth Sci. Ed.) 34, 174–181 (in Chinese with English abstract).
Sun, D.Y., Wu, F.Y., Gao, S., Lu, X.P., 2005. Confirmation of two episodes of A-type granite emplacement during Late Triassic and Early Jurassic in the central Jilin Province, and their constraints on the structural pattern of Eastern Jilin-Heilongjiang Area, China. Earth Sci. Front. 12, 263–275 (in Chinese with English abstract).
Sun, M.D., Xu, Y.G., Wilde, S.A., Chen, H.L., Yang, S.F., 2015. The Permian Dongfanghong island-arc gabbro of the Wandashan Orogen, NE China: implications for Paleo-Pacific subduction. Tectonophysics 659, 122–136.
Sun, S.-S., McDonough, W.F., 1989. Chemical and isotopic systematics of oceanic basalts: implications for mantle composition and processes. In: In: Saunders, A.D., Norry, M.J. (Eds.), Magmatism in Ocean Basins, vol. 42. Geological Society of Special Publication, London, pp. 313–345.
Tang, J., Xu, W.L., Wang, F., Zhao, S., Wang, W., 2015. Early Mesozoic southward subduction history of the Mongol–Okhotsk oceanic plate: evidence from geochronology and geochemistry of Early Mesozoic intrusive rocks in the Erguna Massif, NE China. Gondwana Res. http://dx.doi.org/10.1016/j.gr.2014.12.010.
Tatsumi, Y., Hamilton, D.L., Nesbitt, R.W., 1986. Chemical characteristics of fluid phase released from a subducted lithosphere and origin of arc magmas: evidence from high pressure experiments and natural rocks. J. Volcanol. Geoth. Res. 29, 293–309.
Tu, X.L., Zhang, H., Deng, W.F., Ling, M.X., Liang, H.Y., Liu, Y., Sun, W.D., 2011. Application of RESOlution in-situ laser ablation ICP-MS in trace element analyses. Geochimica 40, 83–98 (in Chinese with English abstract).
Wang, F., Xu, W.L., Meng, E., Cao, H.H., Gao, F.H., 2012. Early Paleozoic amalgamation of the Songnen-Zhangguangcai Range and Jiamusi massifs in the eastern segment of the Central Asian Orogenic Belt: geochronological and geochemical evidence from granitoids and rhyolites. J. Asian Earth Sci. 49, 234–248.
Wang, F., Xu, W.L., Xu, Y.G., Gao, F.H., Ge, W.C., 2015. Late Triassic bimodal igneous rocks in eastern Heilongjiang Province, NE China: implications for the initiation of subduction of the Paleo-Pacific Plate beneath Eurasia. J. Asian Earth Sci. 97, 406–423.
Wang, F., Xu, W.L., Ge, W.C., Yang, H., Pei, F.P., Wu, W., 2016. The offset distance of the Dunhua-Mishan Fault: constraints from Paleozoic-Mesozoic magmatism within the Songnen-Zhangguangcai Range, Jiamusi, and Khanka massifs. Acta Petrol. Sin. 32 (4), 1129–1140.
Wilde, S.A., 2015. Final amalgamation of the Central Asian Orogenic Belt in NE China: paleo-Asian Ocean closure versus Paleo-Pacific plate subduction – a review of the evidence. Tectonophysics. http://dx.doi.org/10.1016/j.tecto.2015.05.006.
Wilson, M., 1989. Igneous Petrogenesis. Unwin Hyman, London, pp. 191–373.
Windley, B.F., Alexeiev, D., Xiao, W.J., Kröner, A., Badarch, G., 2007. Tectonic models for accretion of the Central Asian Orogenic belt. J. Geol. Soc. Lond. 164, 31–47.
Wu, F.Y., Sun, D.Y., Li, H.M., Jahn, B.M., Wilde, S.A., 2002. A-type granites in northeastern China: age and geochemical constraints on their petrogenesis. Chem. Geol. 187, 143–173.
Wu, F.Y., Zhao, G.C., Sun, D.Y., Wilde, S.A., Yang, J.H., 2007a. The Hulan Group: its role in the evolution of the Central Asian Orogenic Belt of NE China. J. Asian Earth Sci. 30, 542–556.
Wu, F.Y., Li, X.H., Zheng, Y.F., Gao, S., 2007b. Lu-Hf isotopic systematics and their applications in petrology. Acta Petrol. Sin. 23, 185–220 (in Chinese with English abstract).
Wu, F.Y., Sun, D.Y., Ge, W.C., Zhang, Y.B., Grant, M.L., Wilde, S.A., Jahn, B.M., 2011. Geochronology of the Phanerozoic granitoids in northeastern China. J. Asian Earth Sci. 41, 1–30.
Wu, P.F., Sun, D.Y., Wang, T.H., Gou, J., Li, R., Liu, W., Liu, X.M., 2013. Chronology, geochemical characteristic and petrogenesis analysis of diorite in Helong of Yanbian Area, NE China. Geol. J. Chin. Univ. 19, 600–610 (in Chinese with English abstract).
Xiao, W.J., Windley, B., Hao, J., Zhai, M.G., 2003. Accretion leading to collision and the Permian Solonker suture, Inner Mongolia, China: termination of the Central Asian Orogenic Belt. Tectonics 2002TC001484.
Xu, W.L., Ji, W.Q., Pei, F.P., Meng, E., Yu, Y., Yang, D.B., Zhang, X.Z., 2009. Triassic volcanism in eastern Heilongjiang and Jilin Provinces, NE China: chronology, geochemistry, and tectonic implications. J. Asian Earth Sci. 34, 392–402.
Xu, W.L., Pei, F.P., Wang, F., Meng, E., Ji, W.Q., Yang, D.B., Wang, W., 2013a. Spatial–temporal relationships of Mesozoic volcanic rocks in NE China: constraints on tectonic overprinting and transformations between multiple tectonic regimes. J. Asian Earth Sci. 74, 167–193.
Xu, W.L., Wang, F., Pei, F.P., Meng, E., Tang, J., Xu, M.J., Wang, W., 2013b. Mesozoic tectonic regimes and regional ore-forming background in NE China: constraints from spatial and temporal variations of Mesozoic volcanic rock associations. Acta Petrol. Sin. 29, 339–353 (in Chinese with English abstract).
Xu, Y.G., Ma, J.L., Huang, X.L., Iizuka, Y., Chung, S.L., Wang, Y.B., Wu, X.Y., 2004. Early Cretaceous gabbroic complex from Yinan, Shandong Province: petrogenesis and mantle domains beneath the North China Craton. Int. J. Earth Sci. 93, 1025–1041.
Xu, Y.G., 2014. Recycled oceanic crust in the source of 90–40 Ma basalts in North and Northeast China: evidence, provenance and significance. Geochim. Cosmochim. Acta 143, 49–67.
Yang, H., Ge, W.C., Zhao, G.C., Yu, J.J., Zhang, Y.L., 2015. Early Permian-Late Triassic granitic magmatism in the Jiamusi-Khanka Massif, eastern segment of the Central Asian Orogenic Belt and its implications. Gondwana Res. 27, 1509–1533.
Yang, J.H., Wu, F.Y., Shao, J., Wilde, S.A., Xie, L.W., Liu, X.M., 2006. Constraints on the timing of uplift of the Yanshan Fold and Thrust Belt, North China. Earth Planet. Sci. Lett. 246, 336–352.
Yang, J.H., Fu, Y., Wu, F.Y., Wilde, S.A., Xie, L.W., Yang, Y.H., Liu, X.M., 2007. Tracing magma mixing in granite genesis: in situ U-Pb dating and Hf-isotope analysis of zircons. Contrib. Miner. Petrol. 153, 177–190.
Yu, J.J., Wang, F., Xu, W.L., Gao, F.H., Pei, F.P., 2012. Early Jurassic mafic magmatism in the Lesser Xing'an–Zhangguangcai Range, NE China, and its tectonic implications: constraints from zircon U-Pb chronology and geochemistry. Lithos 142–143, 256–266.
Zhang, C., Guo, W., Xu, Z.Y., Liu, Z.H., Liu, Y.J., Lei, C.C., 2014. Study on geochronology, petrogenesis and tectonic implications of monzogranite from the Yanbian area, eastern Jilin Province. Acta Petrol. Sin. 30, 512–526 (in Chinese with English abstract).
Zhang, S.H., Zhao, Y., Kröner, A., Liu, X.M., Xie, L.W., Chen, F.K., 2009. Early Permian plutons from the northern North China Block: constraints on continental arc evolution and convergent margin magmatism related to the Central Asian Orogenic Belt. Int. J. Earth Sci. 98, 1441–1467.
Zhang, Y.B., Wu, F.Y., Wilde, S.A., Zhai, M.G., Lu, X.P., Sun, D.Y., 2004. Zircon U-Pb ages and tectonic implications of 'Early Paleozoic' granitoids at Yanbian, Jilin Province, northeast China. The Island Arc 13, 484–505.

Zhao, C.J., Peng, Y.J., Dang, Z.X., Zhang, Y.P., Zhu, Q., Xiu, Y.Z., Wang, Z.F., Tai, C.B., Gu, F., Zhang, J.F., Zheng, C.Z., Dang, Y.S., 1996. The Structural Framework and Crustal Evolution in Eastern Jilin and Heilongjiang Provinces. Liaoning University Press, Shenyang, pp. 1–186 (in Chinese with English abstract).

Zhao, Y., Yang, Z.Y., Ma, X.H., 1994. Geotectonic transition from Paleoasian system and paleotethyan system to Paleopacific active continental margin in Eastern Asia. Sci. Geol. Sin. 29, 105–119 (in Chinese with English abstract).

Zhao, Y., Chen, B., Zhang, S.H., Liu, J.M., Liu, J., Pei, J.L., 2010. Pre-Yanshanian geological events in the northern margin of the North China Craton and its adjacent areas. Geol. Chin. 37, 900–915 (in Chinese with English abstract).

Zhou, J.B., Wilde, S.A., Zhang, X.Z., Zhao, G.C., Zheng, C.Q., Wang, Y.J., Zhang, X.H., 2009. The onset of Pacific margin accretion in NE China: evidence from the Heilongjiang high-pressure metamorphic belt. Tectonophysics 478, 230–246.

Zhou, J.B., Cao, J.L., Wilde, S.A., Zhao, G.C., Zhang, J.J., Wang, B., 2014. Paleo-Pacific subduction-accretion: evidence from Geochemical and U-Pb zircon dating of the Nadanhada accretionary complex, NE China. Tectonics 33, 2444–2466. http://dx.doi.org/10.1002/2014TC003637.